The transcriptome of aneuploidy-induced senescent cells reveals interaction with the tumour microenvironment and a pro-survival role of Yorkie

Kaustuv Ghosh [1,3], Aishwarya Kunchur[1,3] and Marco Milán[1,2,4 *]

[1]Institute for Research in Biomedicine (IRB Barcelona), The Barcelona Institute of Science and Technology, Baldiri Reixac, 10, 08028 Barcelona, Spain.

[2]Institució Catalana de Recerca i Estudis Avançats (ICREA)

Pg. Lluís Companys 23, 08010 Barcelona, Spain

[3]These two authors contributed equally to this work

[4]Lead Contact

[*] Correspondence: marco.milan@irbbarcelona.org

Phone/Fax: 34 93 4034902/34 93 4037109

Running title: Aneuploidy-induced senescence

Keywords:

Number of figures: 8 (+ 6 supplementary)

Number of figures: 1 (+ 4 supplementary)

Number of characters: 63000 (with spaces)

Author ORCiD/ email id:

Kaustuv Ghosh: 0000-0001-8657-4889 / kaustuv.ghosh@irbbarcelona.org

Aishwarya Kunchur: 0000-0002-0653-6848 / aishwarya.kunchur@irbbarcelona.org

Marco Milán: 0000-0002-7111-6444 / marco.milan@irbbarcelona.org

Abstract

Chromosomal instability (CIN)—an increased rate of changes in chromosome structure and number—is observed in most human carcinomas. *Drosophila* has been instrumental in demonstrating that CIN can act as a source of tumour growth, metastasis, and malignancy through the production of aneuploidy-induced senescent cells. Here we unravel a distinct transcriptional program in these cells, despite their highly heterogeneous chromosome content, and show that most cellular responses to aneuploidy and senescence are regulated at the transcriptional level. The senescence-associated secretory phenotype of aneuploid cells consist of more than 40 secreted proteins. We identify four secreted proteins acting on the neighbouring TME to drive cell death, suppress growth, and block proliferation and demonstrate a pro-survival role of the Hippo-Yorkie pathway in senescent cells. Our data contribute to the identification of potential therapeutic strategies to block CIN-induced tumorigenesis by targeting senescent cells and blocking their ability to interact with the tumour microenvironment.

Short title: Aneuploidy-induced senescence and tumour growth

Teaser: Aneuploidy-induced senescent cells activate the pro-survival Hippo-Yorkie pathway and act on the tumour microenvironment to suppress its growth

Introduction

Chromosomal instability (CIN)—a frequent alteration in chromosome number and structure—is one of the most common forms of genomic instability in cancer. It is prevalent in most solid tumours and is closely associated with chemotherapy resistance, reduced patient survival, and metastasis (*1–6*). Traditionally, CIN has been understood to be a driver of genetic diversity within tumours, mainly through the gradual gain of chromosomes that carry oncogenes and the loss of those containing tumour suppressor genes. However, beyond these slow, progressive changes, CIN can also cause sudden and dramatic alterations in the genome. For example, mis-segregated chromosomes can end up in micronuclei, where they often experience extensive DNA damage. This process, known as chromothripsis, leads to the fragmentation and chaotic rearrangement of chromosomes (*7*). In addition to fuelling cancer progression through both gradual and abrupt mechanisms, CIN also causes cytosolic double-stranded DNA, likely originating from ruptured micronuclei. This DNA is detected by cellular sensors, such as cGAS, which normally activate immune responses. However, cancer cells can exploit this pathway to reshape the tumour microenvironment (TME) in a way that suppresses immune activity and promotes metastasis (*8–10*).

Although low levels of CIN are widely recognized as a driver of cancer, excessive levels can be harmful, leading to cell death and the suppression of tumour growth (*11–14*). In normal cells, CIN often results in aneuploidy—an abnormal number of chromosomes—which can disrupt cell function (*15*). Studies in yeast and human cells have shown that this imbalance alters protein ratios and interferes with key cellular processes like DNA replication, mitosis, and metabolism (*16–18*). One outcome of such metabolic disruption is the production of reactive oxygen species (ROS). Studies in *Drosophila* and human cells have shown that cells with high levels of aneuploidy, involving a large proportion of the genome, typically enter a state of senescence—where they permanently stop dividing and begin releasing inflammatory molecules (*19–22*). These molecules help the mammalian immune system identify and eliminate abnormal cells (*23*). Research in *Drosophila* has further revealed that aneuploidy-induced senescence promotes tumour development. The fly genome is organized into four chromosomes [two autosomes, a sex chromosome pair (X and Y), and a tiny dot-like autosome], and epithelial cells with whole-chromosome aneuploidies (thus impacting a large proportion of the genome) are expelled from tissues as a result of gene dosage and proteome

imbalances, proteostasis failure, and mitochondrial dysfunction (*22*, *24*, *25*). Once extruded, these cells undergo JNK-dependent apoptosis (*22*, *24*, *26*, *27*). When fly aneuploid cells are maintained in the tissue by apoptosis inhibition, they often undergo a JNK-driven transition to a mesenchymal-like state and enter a form of senescence marked by G2 cell cycle arrest (*22*, *28*). Key molecules expressed by senescent cells include the *Drosophila* orthologs of Wnt and IL-6 [Wingless (Wg) and Upd3, respectively], which act on neighbouring cells to drive tumour growth, enhance cell motility, and even affect systemic hormonal signals that prevent developmental maturation and cause organismal death (*24*, *29–31*).

In this study, we used the *Drosophila* epithelial model of CIN-induced tumorigenesis to characterize the transcriptional profile of aneuploidy-induced senescent cells. Despite the highly heterogenous chromosome content of these cells, we unravel a distinct transcriptional program. This unique transcriptional program presents evidence that most cellular responses to aneuploidy and senescence, including cell cycle arrest, activation of autophagy, reorganization of the actin cytoskeleton, and a highly secretory phenotype, are regulated at the transcriptional level. In addition to secreted proteins that promote tumour growth, metastasis, and malignancy, we identified a new role for the cytokine Upd1 in inducing autophagy-driven cell death in the surrounding TME. We also uncovered a role of dIlp8 and ImpL2 (fly orthologs of Relaxin and IGBP7, respectively (*32–34*)) in blocking proliferation in TME cells, and a pro-survival function of the Hippo-Yorkie signalling pathway in aneuploid senescent cells. Overall, our data highlight potential therapeutic strategies to prevent CIN-driven tumour development by targeting aneuploidy-induced senescent cells and disrupting their interactions with the TME.

Results

Cellular responses to aneuploidy and senescence are reflected at the transcriptional level

We used the wing primordium of *Drosophila*—a highly proliferative epithelial monolayer that forms a two-sided epithelial sac (Figure 1A)—as a model system to characterize the transcriptional profile of cells subjected to CIN. CIN was induced by depletion of the spindle assembly checkpoint (SAC) gene *rod* (*rough deal*) using an RNAi form expressed with the GAL4/UAS system (*24*, *26*). The *engrailed-gal4* driver, which is restricted to the posterior (P) compartment of the wing primordium (Figure 1A),

was used to limit the induction of CIN to a defined cell population. One of the most attractive features of this model of CIN is that it facilitates the identification of three well-defined cell populations with distinct behaviours (Figure 1B). On one hand, if apoptosis is blocked by the expression of p35 (a baculovirus protein that binds and represses effector caspases Dcp-1 and Drice (*35*)), aneuploid cells delaminate and become cell cycle-arrested, motile, and highly secretory. These cells can then be tracked with MMP1-GFP, which is a GFP-based transcriptional reporter of JNK (*36*) (Figure 1B, green cells). On the other hand, the epithelial tissue subjected to CIN (the P compartment), which consists of cells that remain largely euploid, enters a hyperplastic program that relies on high mitotic activity and unlimited growth potential (Figure 1B, cells located apically to the green cells). Finally, the anterior (A) compartment of these wing primordia (Figure 1B, cells labelled by the Ci marker in red), which are not subject to CIN and whose cells are euploid, will be treated as the TME. The transcriptional profile of these three cell populations (CIN, aneuploid cells, and TME) was compared to the transcriptional profile of control wing primordia expressing p35 under the control of the *engrailed-gal4* driver. Four distinct biological replicates were analysed. Principal Component Analysis (PCA) revealed significant transcriptomic differences between the five populations, showing strict clustering based on their respective traits (Figure 1C). Interestingly, the aneuploid cell population cluster presented the highest level of difference when compared to the compartment of origin [P(CIN)] or the control tissue [P(Control)]. Consistent with this observation, the aneuploid population showed a higher number of upregulated and downregulated genes than the CIN epithelium (Figure 1D, F, see also Figure S2A). However, there was a certain degree of overlap in the type of genes that changed in these two populations when compared to control tissues. We thus analysed the transcriptional profile that was unique to aneuploid cells. Remarkably, many of the previously observed cellular responses to aneuploidy were reflected at the transcriptional level, as shown by gene set enrichment analysis (GSEA, Figure 1E, Figure S1A, and Table S1). First, high levels of proteotoxic stress caused by unbalanced karyotypes were reflected by strong upregulation of genes involved in autophagy (e.g., *atg4a*, *atg8a*, *atg9*, *atg17*, and *atg18b*) and lysosome function (e.g., *Lamp1*, *Vps13D*, *Vps16A, Vamp7,* and *lqf*). Second, consistent with the activation of the JNK stress signalling pathway as a consequence of mitochondrial dysfunction and ROS (*22*, *27*), many of its target genes (e.g., *mmp1*, *ets21C*, and *scaf*) were strongly upregulated in aneuploid cells (Figure 1E, 2A, and Figure S1A).

Third, the ability of aneuploid cells to become motile through modulation of the actin cytoskeleton and a non-apoptotic role of caspases (*28*, *31*) was reflected by strong upregulation of genes involved in these two processes, as well as in cell motility (e.g., *sqh*, *cortactin*, *rok*, *fak*, *Arpc2-5, hid*, *rpr*, *Dronc*, *Drice*, and *Dcp-1;* Figures 1E, 2A, and Figure S1A). Finally, entry into a senescence-like state [22] was also reflected at the transcriptional level, as shown by strong downregulation of genes involved in cell cycle progression (e.g., *stg*, *cdk1*, *cycA*, and *cycB*) and DNA replication (e.g., *DNA polymerase*, *Orc* and *Mcm* complexes, Figure 1E and 2B), and the clear upregulation of genes involved in secretion (e.g., *Tango 5, 11, Sec 5, 6, 33, 24CD, and Rab 1, 2, 6, 7, 10,* and *35*) and encoding for secreted proteins (Figure 1E, 2A, and S1A). Indeed, 42 out of the 250 most upregulated genes encoded for secreted proteins (Table 1 and S2). These included the systemic signals Upd3 cytokine (involved in CIN-induced invasion and developmental delay (*30*, *31*)), Dilp8 relaxin (mediating developmental delay (*30*, *31*)), Pvf1 (PDGF- and VEGF-related factor 1 involved in driving organ wasting (*38*)) and the mitogenic signals Wg and Wnt6 (*29*), many of them are known targets of JNK. We confirmed the highly secretory phenotype of senescent cells by using three fluorescent reporters to mark the enlargement of the Golgi and the endoplasmic reticulum (ER) compartment, and an increase in the number of exosomes (Figure 2C). The transcriptional profile of aneuploid cells that was shared with CIN comprised genes involved in the activation of ERK and JAK/STAT signalling, previously shown to contribute to various aspects of CIN-induced tumorigenesis, such as growth and invasiveness (*28*, *31*) (Figure 1G and S2B, C). In CIN cells, we observed unique upregulation of the genes involved in DNA damage, consistent with the high propensity of dividing cells subjected to SAC depletion to accumulate lagging or broken chromosomes (Figure S2B, C). Overall, these results indicate that the cellular responses to aneuploidy and senescence are reflected at the transcriptional level, and they reinforce the highly secretory phenotype of aneuploidy-induced senescent cells.

A negative effect of CIN tumours on growth and survival of TME cells

The transcriptional profile of TME cells (cells located in the nearby A compartment and not subject to CIN, Figure 1B) showed the upregulation of genes involved in autophagic cell death and a reduction in translation activity (Figure S3A-C). We next examined the response of the TME (A compartment) to the nearby hyperplastic tissue (P compartment) subject to CIN and additional blockage of the apoptotic pathway at different time points of development. As anticipated, the P compartment showed

a steady increase in size, whereas the size of the A compartment was significantly reduced compared with controls (Figure 3A, quantified in Figure 3B). After eight days of development, the A compartment reached the expected size of a control A compartment, while the P compartment continued to grow. The differential growth dynamics of CIN and TME cell populations were also observed when analysing the ratio of their corresponding sizes [P/A ratio; Figure 3B]. Interestingly, the negative impact of the CIN tissue on the growth dynamics of the A compartment was accompanied by an increase in the number of apoptotic cells labelled by TUNEL staining (Figure 3A, quantified in Figure 3C), a reduction in mitotic activity labelled with pH3 antibody (Figure 3D, quantified in Figure 3C), and a decrease in EdU incorporation (Figure 3E, quantified in Figure 3C). We next addressed whether the observed response of the A compartment to the nearby CIN tissue was driven by any of the signalling molecules secreted by aneuploidy-induced senescent cells (Table 1). Interestingly, Dilp8, a molecule secreted by damaged tissues known to delay development but also to reduce systemic growth by blocking Ecdysone production (*39*, *40*) was among the secreted proteins most upregulated in aneuploidy-induced senescent cells (Figure 2A and Table 1). Using a GFP protein trap reporter, we confirmed the expression of Dilp8 in aneuploidy-induced senescent cells (Figure 4A). Depletion of *dilp8* in the CIN tissue (with a *UAS-RNAi*) restored mitotic activity and EdU incorporation levels, but not the number of apoptotic cells, in the adjacent A compartment (Figure 4B and C, quantified in Figure 4B' and C', Figure S4A, B). Interestingly, Dilp8 overexpression reduced mitotic activity even further (Figure 4C, quantified in Figure 4C'). Since *dilp8* depletion was unable to restore the size of the A compartment (Figure 4D), we searched for additional genes expressed in aneuploidy-induced senescent cells with a known role in inhibiting proliferative growth. None of the 42 most upregulated genes encoding for a secreted protein had a reported role in inhibiting proliferative growth (Table 1). However, we identified ImpL2, an ortholog of IGFBP7 that binds to and inhibits the function of *Drosophila* insulin-like peptides (*41*, *42*) and consequently the growth-promoting PI3K signalling pathway, as the 43th most upregulated gene encoding for a secreted protein in aneuploidy-induced senescent cells (Table S2), an upregulation that was confirmed with a GFP protein trap reporter (Figure 4A). Depletion of *ImpL2* in the CIN tissue (with a *UAS-RNAi*) restored mitotic activity and EdU incorporation levels and reduced the number of apoptotic cells in the adjacent A compartment (Figure 4B and C, quantified in Figure 4B' and C', Figure S4A, B), and ImpL2 overexpression reduced mitotic

activity even further (Figure 4C, quantified in Figure 4C'). As observed in the case of Dilp8, *ImpL2* depletion was unable to restore the size of the A compartment either (Figure 4D), Only co-depletion of *dilp8* and *impL2* was able to dampen, to some extent, the reduction in the size of the A compartment caused by the nearby CIN tissue (Figure 4D). This finding thus points to a redundant role of multiple molecules secreted from aneuploidy-induced senescent cells and compromising the growth of the nearby A compartment. The reduction in the proliferative activity of the A compartment was not observed in those cells abutting the CIN tissue (Figure 3E), thus pointing to a signal originating in the P compartment and counteracting the negative effects of Dilp8 and ImpL2 on proliferation (see below). Indeed, the proliferative activity of these cells relies on the activity of the mitogenic molecule Wg produced by senescent cells (Table 1, (*29*)), as Wg depletion reduced the levels of EdU incorporation in these cells (Figure S5D-E).

A role of cytokine Upd1 in driving autophagic cell death in the nearby TME

Aneuploidy-induced senescent cells also showed upregulation of elements of the JAK/STAT pathway, including ligands (cytokines Upd1, Upd2, and Upd3) and the receptor Domeless (Dome, Figure 5A). We confirmed activation of this pathway with a GFP transcriptional reporter of STAT (STAT-GFP (*43*)). Interestingly, we observed that it was also activated in the nearby A compartment (Figure 5B). We therefore addressed the potential contribution of Upd ligands and the JAK/STAT pathway to the effects of CIN tissues on the nearby TME. Expression of a truncated form of receptor Domeless lacking the intracellular domain in the CIN tissue (Dome-ΔCYT) led to a marked reduction in the levels of STAT-GFP signalling, not only cell autonomously but also in the nearby A compartment (Figure 5B). This finding is consistent with the proposed role of Dome-ΔCYT in blocking JAK/STAT signalling by trapping the Upd ligands and competing with the endogenous receptor (*30*). Interestingly, the non-autonomous reduction in STAT-GFP levels caused by Dome-ΔCYT was accompanied by a decrease in the number of apoptotic cells (Figure 5C, quantified in Figure 5C'). In contrast, depletion of Dome by RNAi, which is expected to block ligand-dependent JAK/STAT signalling in a cell autonomous manner without trapping the Upd ligands, did not affect the neighbouring A compartment (Figure 5C, quantified in Figure 5C'). We found that both transgenes (*UAS-dome-ΔCYT* and *UAS-dome-RNAi*) caused a similar reduction in the size of the P compartment,

most probably caused by the developmental role of the JAK/STAT pathway in regulating the growth of this compartment (*44*). The non-autonomous reduction in the number of apoptotic cells caused by Dome-ΔCYT was also observed in tissues mutant for *hop* (the *Drosophila* JAK ortholog) and upon depletion of the cytokine *upd1* by RNAi in CIN and aneuploid cells (Figure 5C, quantified in Figure 5C'). Most interestingly, depletion of *upd1* also rescued the reduction in the size of the A compartment (Figure 5C'). We observed that depletion of the two other ligands (in larvae mutant for *upd2* and *upd3)* did not have any effect on the levels of apoptosis observed in the A compartment or on its size (Figure 5C, C') and that neither *upd1* depletion nor Dome-ΔCYT expression in CIN tissue ameliorated the non-autonomous reduction in proliferation dynamics (Figure S5A, quantified in Figure S5B). Overexpression of Upd1 in the P compartment of the tumour was able to further increase the extent of cell death observed in the nearby A compartment (Figure 5D, D'), which is consistent with the role of this cytokine in exerting non-autonomous action on the TME to induce apoptosis. In those regions with the highest levels of cDcp-1 staining in the TME, autophagy was induced, as reflected by the accumulation in puncta of an mCherry-tagged Atg8a under the control of the endogenous Atg8a promoter (Atg8a; Figure 5E). Interestingly, this induction was largely dependent on Upd1 derived from CIN tissue, as *upd1* depletion led to a significant reduction in the amount of Atg8a signal in the TME (Figure 5E, E'). Most interestingly, compromising autophagic flux, by supplementing the larval food with chloroquine, led to a significant reduction in the extent of cell death observed in the TME (Figure 5F, F'). Taken together, these results suggest that Upd1 contributes to the reduction in the size of the TME by inducing autophagic cell death.

A survival role of hippo/Yorkie in CIN-induced senescent cells

In CIN-induced tumours, the ability of aneuploid cells to become motile relies on modulation of the actin cytoskeleton and a non-apoptotic role of caspases (*28*, *31*). As mentioned above, activation of the apoptotic pathway in aneuploidy-induced senescent cells was reflected by strong upregulation of genes involved in apoptosis, including the pro-apoptotic genes *hid* and *reaper*, the initiator caspase *Dronc,* and the effector caspases *Drice* and *Dcp-1 (*Figure 6A). The increase in *hid* expression was confirmed by a *hid-lacZ* reporter (Figure 6B). Interestingly, the activity levels of effector Caspases, monitored by the GC3Ai activity reporter (*45*), were relatively high in aneuploidy-induced senescent cells when compared to control tissues (Figure 6B) despite the expression of the p35 baculovirus

protein, a potent inhibitor of these Caspases (*35*). However, there were no pyknotic nuclei in the tissue suggesting that apoptosis execution is indeed actively blocked in these cells. In our search for candidate pathways with well-known pro-survival activity, we observed that many elements of the Hippo/Yorkie signalling cascade, including *crumbs* (*crb*), *fat* (*ft*), *Merlin* (*Mer*), *Ajuba* (*jub*), *kibra*, *hippo* (*hpo*), and *yorkie* (*yki*), were transcriptionally activated in aneuploidy-induced senescent cells (Figure 6A). The activation of Yorkie in these cells was confirmed with the use of GFP-protein traps of Diap1 (DIAP1-GFP), Ajuba (Jub-GFP, an upstream negative regulator of Hippo (*46*)) and Yorkie (Figure 6C, D, and F), and transcriptional reporters of *Diap1* (an E3 ubiquitin ligase regulated by Yorkie and involved in inhibiting Dronc, (*47*)), *bantam* (a miRNA regulated by Yorkie and involved in inhibiting *hid* (*48*, *49*)), and *expanded* [an upstream regulator of the Hippo pathway and Yorkie target (*50*), Figure 6E, S6A]. Yorkie has been previously shown to be activated by JNK (*51*), which is highly active in CIN-induced aneuploid cells and plays a pivotal role in defining their senescent state (*22*). Consistently, the expression levels of Yorkie targets *Diap1* and *bantam* were significantly reduced upon blockage of the JNK pathway by expression of a dominant negative version of JNK (Bsk in *Drosophila* (*52*), Figure 6E, F, quantified in Figure 6E', F'). Given the well-known anti-apoptotic role of the Yorkie pathway, we addressed whether Yorkie depletion had any impact on the survival of CIN tissues. To this end, and based on the developmental role of Yorkie in regulating growth and survival of epithelial tissues (*53*), we searched for a mild *UAS-yorkie-RNAi* transgene. Interestingly, depletion of Yorkie (with the use of this mild transgene) did not have a major effect on the size or survival of p35-overexpressing tissues but did have a mild effect on the size and survival of otherwise wild-type tissues (Figure 7A, C, left panels, and quantified in Figure 7B, D). In contrast, the use of this transgene induced a strong negative impact on the size of CIN tissue, and this reduction was accompanied by a significant increase in the number of apoptotic cells (Figure 7A, C, right panels, and quantified in Figure 7B, D). Taken together, these results indicate that the Hippo/Yorkie pathway acts as an intrinsic anti-apoptotic pathway that contributes to dampening the deleterious effects of CIN and maintaining senescent cells alive despite the activation of the apoptotic pathway. Consistent with the proposal of this intrinsic anti-apoptotic pathway, we observed that by halving the doses of the pro-apoptotic genes *reaper*, *hid* and *grim* (in *Df(H99)/+* individuals, a genetic condition that is haploinsufficient in flies) the levels of cell death observed in CIN tissues were reduced (Figure 7E,

and quantified in Figure 7I), and aneuploid cells, labelled by the expression of MMP1, were maintained in the tissue even in the absence of p35 (Figure 7E and F). These cells were negative for apoptotic markers (Figure 7G) and were not the result of loss of Df(H99) heterozygosity caused by CIN, as they expressed the *bantam-lacZ* reporter located in the homologous chromosome (Figure 7H). Most interestingly, under these circumstances, the tissue also overgrew (Figure 7E, F, and quantified in Figure 7I).

Discussion

The transcriptome of aneuploidy-induced senescence

From flies to mammals, CIN is widely recognized as a driver of cellular senescence, primarily through the generation of highly aneuploid karyotypes (*19–22*), and cellular senescence and its associated senescence-associated secretory phenotype (SASP) are major triggers of inflammation and tumorigenesis (*54*). Here we have characterized the transcriptional profile of aneuploidy-induced senescence in an epithelial model of CIN in *Drosophila* that recapitulates most emerging cellular behaviours observed in mammalian epithelial tissues upon CIN (*10*, *21*, *24–28*, *55–57*). Thus, in fly epithelial tissues subjected to CIN and upon additional blockade of the apoptotic pathway, aneuploid cells are extruded from the epithelium and enter a state of senescence characterized by cell cycle arrest in G2, increased motility, and a highly secretory phenotype that drives the hyperplastic growth of the epithelium in a non-autonomous manner (*58*). Consequently, CIN tissues acquire a tumour-like, unlimited growth potential and highly invasive behaviour. All these processes rely on the activity of the JNK signalling pathway. As it occurs from yeast to mammals, aneuploidy activates autophagy as the primary quality control mechanism for maintaining proteostasis in response to gene dosage imbalance and proteotoxic stress (*59*, *60*). Saturated use of the autophagy machinery in these cells leads to the accumulation of dysfunctional mitochondria as a result of compromised mitophagy, and these mitochondria become active sources of ROS (*22*), which ultimately activate JNK via Ask1 (*27*). The use of the GAL4/UAS system to trigger CIN in only one half of the growing wing epithelium and a GFP transcriptional reporter of JNK (MMP1-GFP, (*36*)) has allowed us to characterize the transcriptional profile of aneuploidy-induced senescent cells, the epithelial layer subjected to CIN that enters a hyperplastic mode of growth, and the nearby wild-type population acting as the TME.

Remarkably, most cellular responses to aneuploidy and senescence are robustly reflected at the transcriptional level, as shown by the up- or down-regulation of a large number of genes involved in any of these responses (Figure 8). Thus, cell cycle progression is locked in these cells by the downregulation of most genes involved in DNA replication (including all subunits of the DNA polymerase, and Orc and Mcm complexes) and G2/M transition (including *Dcdc25*/*stg*, *cdk1*, *cycA*, and *cycB*). The induction of autophagy, a process that delivers its cargo to lysosomes for degradation, is accompanied by the upregulation of many autophagy (*atg4a*, *atg8a*, *atg9*, *atg17,* and *atg18b*) and lysosomal genes (e.g., *Lamp1*, *Vps13D*, *Vps16A, Vamp7,* and *lqf*). Similarly, the reported ability of aneuploid cells to become motile through modulation of the actin cytoskeleton is accompanied by the upregulation of many actin cytoskeleton proteins, including Sqh, Cortactin, Rok, Fak, and Arpc2-5. One of the most remarkable properties of senescent cells is the SASP (*61*). Our transcriptomic analysis has unravelled a significant upregulation of genes involved in secretion (e.g., *Tango 5, 11, Sec 5, 6, 33, 24CD,* and *Rab 1, 2, 6, 7, 10,* and *35*), reinforced with the use of cellular reporters to unveil an enlarged secretory apparatus, and has allowed us to identify all the elements of the SASP, where 42 out of the 200 most upregulated genes in these cells encode for secreted proteins (Table S2).

The SASP acts on the TME

In our fly epithelial model of CIN, senescent cells show a remarkable ability to act at a paracrine, autocrine, and systemic level to drive tumour growth, invasiveness, and malignancy, respectively [57]. They exert their action through elements of the SASP, including mitogenic molecules Wg and Wnt6, Matrix metalloproteinase MMP1, and cytokines such as Upd3. Here we identify a new axis of interaction between senescent cells with the nearby TME (Figure 8). While CIN tissue enters a hyperplastic mode of growth in response to the mitogenic molecules Wg and Wnt6 secreted by senescent cells, the nearby TME shows growth arrest, which is accompanied by a reduction in proliferative activity and an increase in the number of apoptotic cells. We identified three distinct components of the SASP driving the observed non-autonomous effects on the TME: the Relaxin-like molecule Dilp8, the Insulin-like growth factor antagonist ImpL2 (the fly ortholog of IGFBP-7), and the cytokine Upd1. While Dilp8 and ImpL2 were shown to be required and sufficient to drive the non-autonomous reduction in proliferative activity, Upd1 was found to be responsible for the reduction in

growth and increase in apoptotic levels of the TME. We present evidence that Upd1 exerts its action by triggering the JAK/STAT signalling pathway and by inducing autophagic cell death. These data expand the repertoire of signalling activities exerted by senescent cells and provide another example of non-cell-autonomous autophagy induction in the TME (*62*). Whether CIN tissues also engage surrounding TME as active contributors to their unlimited growth potential through nutrient-generating autophagy remains to be elucidated.

An anti-apoptotic role of Yorkie in senescent cells

Drosophila CIN tissues are exposed to the activation of pro-apoptotic pathways JNK and JAK/STAT that lead to the elimination of aneuploid cells in the tissue (*24*, *31*). It is the blockage of the apoptotic pathway by the expression of the baculovirus protein p35 what unravels a subversive role of JNK in driving cellular senescence, and JAK/STAT in promoting cell motility. However, the apoptotic pathway is not completely blocked under these conditions as shown by the high activity levels of effector caspases in the tissue, which have been shown to contribute in a non-apoptotic manner to the invasive behaviour of aneuploid cells. These results point to the presence of an endogenous pathway that counteracts the pro-apoptotic activities of JNK and JAK/STAT. Similar to how senescent cells in mammals resist normal apoptotic pathways through expression of the Bcl2 anti-apoptotic protein (*63*), our results indicate that the Hippo/Yorkie pathway plays an analogous role in senescent fly cells (Figure 8). Activation of this pathway is most probably the result of JNK activation and cellular tension positively regulating the cortical localization of Ajuba expression to sequester Warts, thus allowing Yorkie to translocate into the nucleus and drive gene expression (*51*, *64*). Although DIAP1 (a negative regulator of the initiator Caspase Dronc (*47*)) or bantam miRNA (which acts negatively on the hid 3'UTR (*65*)) could be two potential target genes of Yorkie that block the death of senescent cells, the finding that effector caspases show high activity in these cells suggests that Yorkie negatively impinges on the apoptotic pathway even at the level of cell death execution. These experimental data contribute to the identification of Yorkie as a potential therapeutic strategy to block CIN-induced tumorigenesis by targeting senescent cells.

Materials and Methods

Fly maintenance, husbandry and transgene expression

Strains of *Drosophila melanogaster* were maintained on standard medium (4% glucose, 55 g/L yeast, 0.65% agar, 28 g/L wheat flour, 4 ml/L propionic acid, and 1.1 g/L nipagin) at 25°C in light/dark cycles of 12 h. The resulting larvae after the egg laying (AEL) at 25°C were either transferred to 29°C, or maintained at 25°C for specific experiments as mentioned in the figures, and were dissected on the day AEL as mentioned in the figures. The sex of experimental larvae was not considered relevant to this study and was not determined. The strains used are summarized in Table S4.

Standard induction of CIN, and endogenous labelling of different tissue subpopulations for transcriptomic analysis

Virgin female flies carrying *UAS-myrT, MMP1-GFP* transgenes were crossed with males carrying either *en-GAL4, UAS-p35* (Control) or *en-GAL4, UAS-p35, UAS-rod*^{RNAi} (CIN) transgenes. Fertilized females were allowed to lay eggs at 25˚C, and the resulting larvae were switched to 29˚C 24 h AEL. Wing imaginal discs were then dissected after either 5 days (in case of control) or 7 days (in case of CIN) of induction at 29°C. Wing imaginal discs (40–50 in case of controls, and 30–40 in case of CIN) were cleaned in ice-cold 1X PBS and were incubated in 10X trypsin-EDTA (Sigma-Aldrich) at room temperature (RT) for 1 h, with regular nutation, and gentle pipetting. The single cell suspension was then subjected to centrifugation at 2500*g* for 2.5 min. The supernatant was gently removed, and the cells were stained with 1 ml of 1ug/ml of DAPI solution for 10 min at 4°C in low-light conditions, after resuspending the cell pellet. The cells were immediately transferred to flow-tubes, and FACS sorting was carried out on the different tissue subpopulations.

FACS sorting of different tissue subpopulations

Flow cytometric experiments were carried out using a FACS Aria Fusion sorter (Beckton Dickinson, San Jose, California) equipped with a 4-laser configuration (405-488-561-640nm). Single cells were gated according to scatter parameters, using FSC width to avoid doublets. Dead cells were excluded using DAPI as a viability marker; only live single cells were analysed, and these were sorted on the basis of their fluorescence pattern. For sorting different CIN subpopulations from CIN tissues, P(Aneuploid) cells were distinguished as GFP+ RFP+ cells and P(CIN) cells as GFP- RFP+ cells, and the remaining GFP- RFP- cells were labelled as A(Aneuploid) cells. Similarly, for sorting the two

subpopulations from the control tissues, RFP+ cells were attributed as P(control), while the RFP- cells were attributed as A(control). Fluorescence of GFP was detected using blue (488 nm) laser excitation and collecting green fluorescence using a 530/30 BP filter. RFP fluorescence was obtained using green-yellow laser excitation (561 nm) and collecting fluorescence using a 610/20 BP filter. A dot plot combining GFP and RFP emission on single live cells was used to select them for sorting into 1.5 ml Eppendorf tubes. A 70 µm nozzle was used to minimize the sorted volume into collection vials. During the entire experiment, the cells were under 300 RPM agitation and were maintained at 4ºC. For each subpopulation, 30000 cells were collected in RNase-free 1.5 ml microcentrifuge tubes containing 10 µl of freshly prepared 2X Lysis Buffer following the methods from (*66*).

RNA purification, library preparation, and bulk RNA-sequencing

Total RNA from a total of 4 replicates of 5 distinct subpopulations was then purified at the IRB Barcelona Functional Genomics Core Facility, as described in (*66*). mRNA was isolated from total RNA using the NEBNext Poly(A) mRNA Magnetic Isolation Module Kit (New England Biolabs). NGS libraries were prepared from the purified mRNA using the NEBNext Ultra II RNA Library Prep Kit for Illumina (New England Biolabs). A total of 18 cycles of PCR amplification were applied to all libraries. The final libraries were quantified using the Qubit dsDNA HS assay (Invitrogen) and quality controlled with the Bioanalyzer 2100 DNA HS assay (Agilent). An equimolar pool was prepared with the 20 libraries and submitted for sequencing at the *Centro Nacional de Análisis Genómico* (CNAG). A final quality control by qPCR was performed by the sequencing provider before paired-end 150 nt sequencing on a NovaSeq6000 S4 (Illumina). More than 275 Gbp of reads were produced, with a minimum of 39 million paired-end reads per sample.

Data processing

Adapters from reads were removed using trim galore (v.0.6.7) (https://github.com/FelixKrueger/TrimGalore) with default parameters. Resulting reads were aligned to the dm6 *D. melanogaster* genome version using STAR (v.2.7.10a) (*67*). The count matrix was generated in R (https://www.R-project.org/) through the function "featureCounts" of the Rsubread package (*68*).

Differential expression

Differential expression was performed using the DESeq2 package (*69*). For plotting purposes and generating principal components, the count matrix was normalized using the "vst" function.

Gene set enrichment analysis

Gene set enrichment analysis was performed using the roastgsa package (*70*). GO and KEGG pathways were downloaded using the org.Dm.eg.db package.

Immunohistochemistry

Larvae were selected according to the day AEL mentioned in the individual figures, and wing imaginal discs were dissected in phosphate-buffered saline (PBS), fixed for 20 min in 4% formaldehyde in PBS, and stained with antibodies in PBS with 0.3% BSA, 0.2% Triton X-100. The antibodies and reagents used in this study are summarized in Table S4.

DNA synthesis

The Click-iT™ Plus EdU Alexa Fluor™ 647 Imaging Kit from Invitrogen (C10640) was used to measure DNA synthesis (S phase) in proliferating cells, following the manufacturer's instructions. EdU (5-ethynyl-2´-deoxyuridine) provided in the kit is a nucleoside analogue of thymidine and is incorporated into DNA during active DNA synthesis. Time of incubation with EdU: 15 min

TUNEL

Larvae were dissected in cold 1X PBS and fixed in 4% FA for 20 min. After fixation, three fast washes with PBT 0.3% Triton (PBS 1%, Triton X-100 0.3%) followed by four 15-min washes with PBT 0.3% Triton were performed. The samples were blocked with BBT (0.3% BSA, 0.3% Triton X-100) for 1 h rotating at RT and then incubated overnight with the primary antibody at 4℃. The next day, samples were subjected to three fast washes with PBT 0.3% Triton, and then they were washed four more times with PBT 0.3% Triton for 20 min each, followed by incubation with secondary antibodies diluted in BBT for 90 min rotating in the dark at RT. After incubation, the samples were subjected to three rounds of fast washes with PBT 0.3% Triton and four 20-min washes with PBT 0.3%. Samples were kept in BBT blocking overnight at 4ºC. The following day, samples were permeabilized with 495 µl of

100 mM Na-Citrate and 2.5 µl of 20% TritonX for 30 min at 65ºC and then subjected to three fast washes with PBT 0.3% Triton. They were then incubated twice for 5 min at RT with 50 µl of Equilibration buffer. Then 51 µl of TUNEL reaction mix (50 µl of TUNEL reaction buffer Component A, 1 µl TdT Enzyme, Biotium) was added and the samples were incubated for 2 h at RT. After incubation, the samples were subjected to three fast washes with PBT 0.3% Triton, followed by a 30-min incubation with DAPI at RT. Finally, three fast washes and three 10-min washes with PBT 0.3% Triton were performed. Stained tissues were kept in mounting media.

Confocal microscopy.

Samples were analysed using the following confocal microscopes: STELLARIS Confocal Platform with White Light Laser (Leica Microsystems), LSM 780 Zeiss, and LSM880 Zeiss fitted with a Fast Airyscan module (Carl Zeiss). Z-stacks were acquired using either the laser scanning confocal mode or the High-Resolution mode (Airyscan). Image acquisition was done with 20x, 25x, 40x, 63x, and 100x lenses. The most representative image is shown in all experiments.

Chloroquine treatment

Flies of desired genotypes were crossed and set up at 25°C and shifted to 29°C 8 h AEL. After 48 h at 29°C, a working concentration of 3 mg/ml of chloroquine (with water as controls) was added to the food. Larvae were processed 72 h thereafter. Experimental flies and control individuals were grown in parallel.

Tissue size, cell death and mitotic activity

The sizes of the whole wing disc (based on DAPI staining) and the anterior (A) and posterior (P) compartments (based on Ci expression) were measured manually using Fiji Software (NIH, USA) on apical sections (epithelium) of the wing disc obtained using a Zeiss LSM780 confocal microscope. For comparisons of the area of the A or the P compartments, the area of the respective compartments in the nubbin domain was considered, except in Figure 5D, and the measurement of the size was normalized to the size of the control compartment. The left column of each graph represents the genotype which was considered as the control. The area of the signal to be quantified (TUNEL, cDcp-1, EdU, pH3, and mCh-Atg8) was set by manually adjusting the threshold and normalized to the area

of the indicated larval territory (A or P compartments within the wing pouch) after making a maximum intensity Z-Projection, except in the case of Figure 5D, where a single basal-most stack was quantified by using the threshold function.

Statistical analysis

Statistical analysis was performed by either One-way ANOVA when comparing more than two experimental groups or an unpaired equal-variance two-tailed Student's t-test when comparing the difference in means of a single experimental group with a control. Differences were considered significant when p values were less than 0.0001 (****), 0.001 (***), 0.01 (**), or 0.05 (*). All genotypes included in each histogram or scatter plot were subjected to the same experimental conditions (temperature and time of transgene induction) and analysed in parallel. Mean values and standard deviations were calculated, and the corresponding statistical analysis and graphical representations were carried out with GraphPad Prism 10.0 statistical software.

Data availability

Materials generated for the study are available from the corresponding author on request. Source data are provided with this paper. The raw and processed RNAseq data have been deposited in the GEO database. This information would be made available upon justified request to the corresponding author.

References

1. B. Nguyen, C. Fong, A. Luthra, S. A. Smith, R. G. DiNatale, S. Nandakumar, H. Walch, W. K. Chatila, R. Madupuri, R. Kundra, C. M. Bielski, B. Mastrogiacomo, M. T. A. Donoghue, A. Boire, S. Chandarlapaty, K. Ganesh, J. J. Harding, C. A. Iacobuzio-Donahue, P. Razavi, E. Reznik, C. M. Rudin, D. Zamarin, W. Abida, G. K. Abou-Alfa, C. Aghajanian, A. Cercek, P. Chi, D. Feldman, A. L. Ho, G. Iyer, Y. Y. Janjigian, M. Morris, R. J. Motzer, E. M. O'Reilly, M. A. Postow, N. P. Raj, G. J. Riely, M. E. Robson, J. E. Rosenberg, A. Safonov, A. N. Shoushtari, W. Tap, M. Y. Teo, A. M. Varghese, M. Voss, R. Yaeger, M. G. Zauderer, N. Abu-Rustum, J. Garcia-Aguilar, B. Bochner, A. Hakimi, W. R. Jarnagin, D. R. Jones, D. Molena, L. Morris, E. Rios-Doria, P. Russo, S. Singer, V. E. Strong, D. Chakravarty, L. H. Ellenson, A. Gopalan, J. S. Reis-Filho, B. Weigelt, M. Ladanyi, M. Gonen, S. P. Shah, J. Massague, J. Gao, A. Zehir, M. F. Berger, D. B. Solit, S. F. Bakhoum, F. Sanchez-Vega, N. Schultz, Genomic characterization of metastatic patterns from prospective clinical sequencing of 25,000 patients. *Cell*. **185**, 563-575.e11 (2022).

2. A. J. X. Lee, D. Endesfelder, A. J. Rowan, A. Walther, N. J. Birkbak, P. A. Futreal, J. Downward, Z. Szallasi, I. P. M. Tomlinson, M. Howell, M. Kschischo, C. Swanton, Chromosomal Instability Confers Intrinsic Multidrug Resistance. *Cancer Res.* **71**, 1858–1870 (2011).

3. E. van Dijk, T. van den Bosch, K. J. Lenos, K. El Makrini, L. E. Nijman, H. F. B. van Essen, N. Lansu, M. Boekhout, J. H. Hageman, R. C. Fitzgerald, C. J. A. Punt, J. B. Tuynman, H. J. G. Snippert, G. J. P. L. Kops, J. P. Medema, B. Ylstra, L. Vermeulen, D. M. Miedema, Chromosomal copy number heterogeneity predicts survival rates across cancers. *Nat. Commun.* **12**, 3188 (2021).

4. D. A. Lukow, E. L. Sausville, P. Suri, N. K. Chunduri, A. Wieland, J. Leu, J. C. Smith, V. Girish, A. A. Kumar, J. Kendall, Z. Wang, Z. Storchova, J. M. Sheltzer, Chromosomal instability accelerates the evolution of resistance to anti-cancer therapies. *Dev. Cell*. **56**, 2427-2439.e4 (2021).

5. M. R. Ippolito, V. Martis, S. Martin, A. E. Tijhuis, C. Hong, R. Wardenaar, M. Dumont, J. Zerbib, D. C. J. J. Spierings, D. Fachinetti, U. Ben-David, F. Foijer, S. Santaguida, Gene copy-number changes and chromosomal instability induced by aneuploidy confer resistance to chemotherapy. *Dev. Cell*. **56**, 2440-2454.e6 (2021).

6. T. Davoli, A. W. Xu, K. E. Mengwasser, L. M. Sack, J. C. Yoon, P. J. Park, S. J. Elledge, Cumulative Haploinsufficiency and Triplosensitivity Drive Aneuploidy Patterns and Shape the Cancer Genome. *Cell*. **155**, 948–62 (2013).

7. P. J. Stephens, C. D. Greenman, B. Fu, F. Yang, G. R. Bignell, L. J. Mudie, E. D. Pleasance, K. W. Lau, D. Beare, L. A. Stebbings, S. McLaren, M.-L. Lin, D. J. McBride, I. Varela, S. Nik-Zainal, C. Leroy, M. Jia, A. Menzies, A. P. Butler, J. W. Teague, M. A. Quail, J. Burton, H. Swerdlow, N. P. Carter, L. A. Morsberger, C. Iacobuzio-Donahue, G. A. Follows, A. R. Green, A. M. Flanagan, M. R. Stratton, P. A. Futreal, P. J. Campbell, Massive Genomic Rearrangement Acquired in a Single Catastrophic Event during Cancer Development. *Cell*. **144**, 27–40 (2011).

8. J. Li, M. J. Hubisz, E. M. Earlie, M. A. Duran, C. Hong, A. A. Varela, E. Lettera, M. Deyell, B. Tavora, J. J. Havel, S. M. Phyu, A. D. Amin, K. Budre, E. Kamiya, J.-A. Cavallo, C. Garris, S. Powell, J. S. Reis-Filho, H. Wen, S. Bettigole, A. J. Khan, B. Izar, E. E. Parkes, A. M. Laughney, S. F. Bakhoum, Non-cell-autonomous cancer progression from chromosomal instability. *Nature*. **620**, 1080–1088 (2023).

9. J. Li, M. A. Duran, N. Dhanota, W. K. Chatila, S. E. Bettigole, J. Kwon, R. K. Sriram, M. P. Humphries, M. Salto-Tellez, J. A. James, M. G. Hanna, J. C. Melms, S. Vallabhaneni, K. Litchfield, I. Usaite, D. Biswas, R. Bareja, H. W. Li, M. L. Martin, P. Dorsaint, J.-A. Cavallo, P. Li, C. Pauli, L. Gottesdiener, B. J. DiPardo, T. J. Hollmann, T. Merghoub, H. Y. Wen, J. S. Reis-Filho, N. Riaz, S.-S. M. Su, A. Kalbasi, N. Vasan, S. N. Powell, J. D. Wolchok, O. Elemento, C. Swanton, A. N. Shoushtari, E. E. Parkes, B. Izar, S. F. Bakhoum, Metastasis and Immune Evasion from Extracellular cGAMP Hydrolysis. *Cancer Discov.* **11**, 1212–1227 (2021).

10. S. F. Bakhoum, B. Ngo, A. M. Laughney, J.-A. Cavallo, C. J. Murphy, P. Ly, P. Shah, R. K. Sriram, T. B. K. Watkins, N. K. Taunk, M. Duran, C. Pauli, C. Shaw, K. Chadalavada, V. K. Rajasekhar, G. Genovese, S. Venkatesan, N. J. Birkbak, N. McGranahan, M. Lundquist, Q. LaPlant, J. H. Healey, O. Elemento, C. H. Chung, N. Y. Lee, M. Imielenski, G. Nanjangud, D. Pe'er, D. W. Cleveland, S. N. Powell, J. Lammerding, C. Swanton, L. C. Cantley, Chromosomal instability drives metastasis through a cytosolic DNA response. *Nature*. **553**, 467–472 (2018).

11. A. D. Silk, L. M. Zasadil, A. J. Holland, B. Vitre, D. W. Cleveland, B. A. Weaver, Chromosome missegregation rate predicts whether aneuploidy will promote or suppress tumors. *Proc Natl Acad Sci U S A*. **110**, E4134-41 (2013).

12. K. M. Godek, M. Venere, Q. Wu, K. D. Mills, W. F. Hickey, J. N. Rich, D. A. Compton, Chromosomal Instability Affects the Tumorigenicity of Glioblastoma Tumor-Initiating Cells. *Cancer Discov.* **6**, 532–545 (2016).

13. B. a a Weaver, A. D. Silk, C. Montagna, P. Verdier-Pinard, D. W. Cleveland, Aneuploidy acts both oncogenically and as a tumor suppressor. *Cancer Cell*. **11**, 25–36 (2007).

14. J. Monserrat, C. Morales Torres, L. Richardson, T. S. Wilson, H. Patel, M.-C. Domart, S. Horswell, O.-R. Song, M. Jiang, M. Crawford, M. Bui, Y. Dalal, P. Scaffidi, Disruption of the MSL complex inhibits tumour maintenance by exacerbating chromosomal instability. *Nat. Cell Biol.* **23**, 401–412 (2021).

15. S. L. Thompson, D. A. Compton, Proliferation of aneuploid human cells is limited by a p53-dependent mechanism. *J Cell Biol*. **188**, 369–381 (2010).

16. S. Santaguida, A. Amon, Short- and long-term effects of chromosome mis-segregation and aneuploidy. *Nat Rev Mol Cell Biol*. **16**, 473–485 (2015).

17. J. Zhu, H.-J. Tsai, M. R. Gordon, R. Li, Cellular Stress Associated with Aneuploidy. *Dev. Cell*. **44**, 420–431 (2018).

18. R. Li, J. Zhu, Effects of aneuploidy on cell behaviour and function. *Nat. Rev. Mol. Cell Biol.* (2022), doi:10.1038/s41580-021-00436-9.

19. M. Barroso-Vilares, J. C. Macedo, M. Reis, J. D. Warren, D. Compton, E. Logarinho, Small-molecule inhibition of aging-associated chromosomal instability delays cellular senescence. *EMBO Rep.* **21**, e49248 (2020).

20. J. C. Macedo, S. Vaz, B. Bakker, R. Ribeiro, P. L. Bakker, J. M. Escandell, M. G. Ferreira, R. Medema, F. Foijer, E. Logarinho, FoxM1 repression during human aging leads to mitotic decline and aneuploidy-driven full senescence. *Nat. Commun.* **9**, 2834 (2018).

21. S. Santaguida, A. Richardson, D. R. Iyer, O. M'Saad, L. Zasadil, K. A. Knouse, Y. L. Wong, N. Rhind, A. Desai, A. Amon, Chromosome Mis-segregation Generates Cell-Cycle-Arrested Cells with Complex Karyotypes that Are Eliminated by the Immune System. *Dev Cell*. **41**, 638-651 e5 (2017).

22. J. Joy, L. Barrio, C. Santos-Tapia, D. Romão, N. N. Giakoumakis, M. Clemente-Ruiz, M. Milán, Proteostasis failure and mitochondrial dysfunction leads to aneuploidy-induced senescence. *Dev. Cell*. **56**, 2043-2058.e7 (2021).

23. R. W. Wang, S. Viganò, U. Ben-David, A. Amon, S. Santaguida, Aneuploid senescent cells activate NF-κB to promote their immune clearance by NK cells. *EMBO Rep.* **22** (2021), doi:10.15252/embr.202052032.

24. A. Dekanty, L. Barrio, M. Muzzopappa, H. Auer, M. Milan, Aneuploidy-induced delaminating cells drive tumorigenesis in Drosophila epithelia. *Proc. Natl. Acad. Sci.* **109**, 20549–20554 (2012).

25. M. Clemente-Ruiz, J. M. Murillo-Maldonado, N. Benhra, L. Barrio, L. Perez, G. Quiroga, A. R. Nebreda, M. Milan, L. Pérez, G. Quiroga, A. R. Nebreda, M. Milán, Gene Dosage Imbalance Contributes to Chromosomal Instability-Induced Tumorigenesis. *Dev Cell*. **36**, 290–302 (2016).

26. S. Morais da Silva, T. Moutinho-Santos, C. E. Sunkel, A tumor suppressor role of the Bub3 spindle checkpoint protein after apoptosis inhibition. *J Cell Biol*. **201**, 385–393 (2013).

27. M. Muzzopappa, L. Murcia, M. Milan, M. Milán, M. Milan, Feedback amplification loop drives malignant growth in epithelial tissues. *Proc Natl Acad Sci U S A*. **114**, E7291–E7300 (2017).

28. N. Benhra, L. Barrio, M. Muzzopappa, M. Milán, Chromosomal Instability Induces Cellular Invasion in Epithelial Tissues. *Dev. Cell*. **47**, 161-174.e4 (2018).

29. E. Gracia-Latorre, L. Pérez, M. Muzzopappa, M. Milán, A single WNT enhancer drives specification and regeneration of the Drosophila wing. *Nat. Commun.* **13**, 4794 (2022).

30. D. Romão, M. Muzzopappa, L. Barrio, M. Milán, The Upd3 cytokine couples inflammation to maturation defects in Drosophila. *Curr. Biol.* **31**, 1780-1787.e6 (2021).

31. L. Barrio, A.-E. Gaspar, M. Muzzopappa, K. Ghosh, D. Romao, M. Clemente-Ruiz, M. Milán,

Chromosomal instability-induced cell invasion through caspase-driven DNA damage. *Curr. Biol.* **33**, 4446-4457.e5 (2023).

32. A. Garelli, A. M. Gontijo, V. Miguela, E. Caparros, M. Dominguez, Imaginal Discs Secrete Insulin-Like Peptide 8 to Mediate Plasticity of Growth and Maturation. *Science (80-.).* **336**, 579–582 (2012).

33. J. Colombani, D. S. D. S. Andersen, P. Leopold, P. Léopold, Secreted peptide Dilp8 coordinates Drosophila tissue growth with developmental timing. *Science*. **336**, 582–5 (2012).

34. Y. Kwon, W. Song, I. A. Droujinine, Y. Hu, J. M. Asara, N. Perrimon, Systemic Organ Wasting Induced by Localized Expression of the Secreted Insulin/IGF Antagonist ImpL2. *Dev Cell*. **33**, 36–46 (2015).

35. B. A. Hay, T. Wolff, G. M. Rubin, Expression of baculovirus P35 prevents cell death in Drosophila. *Development*. **120**, 2121–2129 (1994).

36. M. Uhlirova, D. Bohmann, JNK- and Fos-regulated Mmp1 expression cooperates with Ras to induce invasive tumors in Drosophila. *EMBO J.* **25**, 5294–304 (2006).

37. A. Figueroa-Clarevega, D. Bilder, Malignant Drosophila Tumors Interrupt Insulin Signaling to Induce Cachexia-like Wasting. *Dev Cell*. **33**, 47–55 (2015).

38. W. Song, S. Kir, S. Hong, Y. Hu, X. Wang, R. Binari, H.-W. Tang, V. Chung, A. S. Banks, B. Spiegelman, N. Perrimon, Tumor-Derived Ligands Trigger Tumor Growth and Host Wasting via Differential MEK Activation. *Dev. Cell*. **48**, 277-286.e6 (2019).

39. J. A. Sanchez, D. Mesquita, M. C. Ingaramo, F. Ariel, M. Milán, A. Dekanty, Eiger/TNFα-mediated Dilp8 and ROS production coordinate intra-organ growth in Drosophila. *PLOS Genet.* **15**, e1008133 (2019).

40. L. Boulan, D. Andersen, J. Colombani, E. Boone, P. Léopold, Inter-Organ Growth Coordination Is Mediated by the Xrp1-Dilp8 Axis in Drosophila. *Dev. Cell*. **49**, 811-818.e4 (2019).

41. N. Arquier, C. Géminard, M. Bourouis, G. Jarretou, B. Honegger, A. Paix, P. Léopold, Drosophila ALS regulates growth and metabolism through functional interaction with insulin-like peptides. *Cell Metab.* **7**, 333–8 (2008).

42. B. Honegger, M. Galic, K. Köhler, F. Wittwer, W. Brogiolo, E. Hafen, H. Stocker, Imp-L2, a putative homolog of vertebrate IGF-binding protein 7, counteracts insulin signaling in Drosophila and is essential for starvation resistance. *J. Biol.* **7**, 10 (2008).

43. E. A. Bach, L. A. Ekas, A. Ayala-Camargo, M. S. Flaherty, H. Lee, N. Perrimon, G. H. Baeg, GFP reporters detect the activation of the Drosophila JAK/STAT pathway in vivo. *Gene Expr Patterns*. **7**, 323–331 (2007).

44. C. Recasens-Alvarez, A. Ferreira, M. Milán, M. Milan, JAK/STAT controls organ size and fate specification by regulating morphogen production and signalling. *Nat Commun*. **8**, 13815 (2017).

45. S. Schott, A. Ambrosini, A. Barbaste, C. Benassayag, M. Gracia, A. Proag, M. Rayer, B. Monier, M. Suzanne, A fluorescent toolkit for spatiotemporal tracking of apoptotic cells in living Drosophila tissues. *Development*. **144**, 3840–3846 (2017).

46. M. Das Thakur, Y. Feng, R. Jagannathan, M. J. Seppa, J. B. Skeath, G. D. Longmore, Ajuba LIM Proteins Are Negative Regulators of the Hippo Signaling Pathway. *Curr. Biol.* **20**, 657–662 (2010).

47. P. Meier, J. Silke, S. J. Leevers, G. I. Evan, The Drosophila caspase DRONC is regulated by DIAP1. *EMBO J.* **19**, 598–611 (2000).

48. B. J. Thompson, S. M. Cohen, The Hippo pathway regulates the bantam microRNA to control cell proliferation and apoptosis in Drosophila. *Cell*. **126**, 767–774 (2006).

49. R. Nolo, C. M. Morrison, C. Tao, X. Zhang, G. Halder, The bantam microRNA is a target of the hippo tumor-suppressor pathway. *Curr Biol*. **16**, 1895–1904 (2006).

50. F. Hamaratoglu, M. Willecke, M. Kango-Singh, R. Nolo, E. Hyun, C. Tao, H. Jafar-Nejad, G. Halder, The tumour-suppressor genes NF2/Merlin and Expanded act through Hippo signalling to regulate cell proliferation and apoptosis. *Nat Cell Biol*. **8**, 27–36 (2006).

51. G. Sun, K. D. Irvine, Ajuba family proteins link JNK to Hippo signaling. *Sci Signal*. **6**, ra81 (2013).

52. H. K. Sluss, Z. Han, T. Barrett, D. C. Goberdhan, C. Wilson, R. J. Davis, Y. T. Ip, A JNK signal transduction pathway that mediates morphogenesis and an immune response in Drosophila. *Genes Dev*. **10**, 2745–2758 (1996).

53. W. Kowalczyk, L. Romanelli, M. Atkins, H. Hillen, C. Bravo González-Blas, J. Jacobs, J. Xie, S. Soheily, E. Verboven, I. M. Moya, S. Verhulst, M. de Waegeneer, L. Sansores-Garcia, L. van Huffel, R. L. Johnson, L. A. van Grunsven, S. Aerts, G. Halder, Hippo signaling instructs ectopic but not normal organ growth. *Science (80-.).* **378** (2022), doi:10.1126/science.abg3679.

54. V. Gorgoulis, P. D. Adams, A. Alimonti, D. C. Bennett, O. Bischof, C. Bishop, J. Campisi, M. Collado, K. Evangelou, G. Ferbeyre, J. Gil, E. Hara, V. Krizhanovsky, D. Jurk, A. B. Maier, M. Narita, L. Niedernhofer, J. F. Passos, P. D. Robbins, C. A. Schmitt, J. Sedivy, K. Vougas, T. von Zglinicki, D. Zhou, M. Serrano, M. Demaria, Cellular Senescence: Defining a Path Forward. *Cell*. **179**, 813–827 (2019).

55. K. Rowald, M. Mantovan, J. Passos, C. Buccitelli, B. R. Mardin, J. O. Korbel, M. Jechlinger, R. Sotillo, Negative Selection and Chromosome Instability Induced by Mad2 Overexpression Delay Breast Cancer but Facilitate Oncogene-Independent Outgrowth. *Cell Rep.* **15**, 2679–2691 (2016).

56. M. S. Levine, B. Bakker, B. Boeckx, J. Moyett, J. Lu, B. Vitre, D. C. Spierings, P. M. Lansdorp, D. W. Cleveland, D. Lambrechts, F. Foijer, A. J. Holland, Centrosome Amplification Is Sufficient to Promote Spontaneous Tumorigenesis in Mammals. *Dev Cell*. **40**, 313-322 e5 (2017).

57. M. Clemente-Ruiz, M. Muzzopappa, M. Milán, M. Milan, Tumor suppressor roles of CENP-E and Nsl1 in Drosophila epithelial tissues. *Cell Cycle*. **13**, 1450–1455 (2014).

58. J. Joy, E. Fusari, M. Milán, Aneuploidy-induced cellular behaviors: Insights from Drosophila. *Dev. Cell*. **59**, 295–307 (2024).

59. S. Stingele, G. Stoehr, Z. Storchova, Activation of autophagy in cells with abnormal karyotype. *Autophagy*. **9**, 246–248 (2013).

60. S. Santaguida, E. Vasile, E. White, A. Amon, Aneuploidy-induced cellular stresses limit autophagic degradation. *Genes Dev*. **29**, 2010–2021 (2015).

61. B. Wang, J. Han, J. H. Elisseeff, M. Demaria, The senescence-associated secretory phenotype and its physiological and pathological implications. *Nat. Rev. Mol. Cell Biol.* **25**, 958–978 (2024).

62. N. S. Katheder, R. Khezri, F. O'Farrell, S. W. Schultz, A. Jain, M. M. Rahman, K. O. Schink, T. A. Theodossiou, T. Johansen, G. Juhasz, D. Bilder, A. Brech, H. Stenmark, T. E. Rusten, Microenvironmental autophagy promotes tumour growth. *Nature*. **541**, 417–420 (2017).

63. N. Martin, N. Popgeorgiev, G. Ichim, D. Bernard, BCL-2 proteins in senescence: beyond a simple target for senolysis? *Nat. Rev. Mol. Cell Biol.* **24**, 517–518 (2023).

64. C. Rauskolb, S. Sun, G. Sun, Y. Pan, K. D. Irvine, Cytoskeletal Tension Inhibits Hippo

Signaling through an Ajuba-Warts Complex. *Cell*. **158**, 143–156 (2014).

65. J. Brennecke, D. R. Hipfner, A. Stark, R. B. Russell, S. M. Cohen, bantam encodes a developmentally regulated microRNA that controls cell proliferation and regulates the proapoptotic gene hid in Drosophila. *Cell*. **113**, 25–36 (2003).

66. E. Gonzalez-Roca, X. Garcia-Albéniz, S. Rodriguez-Mulero, R. R. Gomis, K. Kornacker, H. Auer, Accurate Expression Profiling of Very Small Cell Populations. *PLoS One*. **5**, e14418 (2010).

67. A. Dobin, C. A. Davis, F. Schlesinger, J. Drenkow, C. Zaleski, S. Jha, P. Batut, M. Chaisson, T. R. Gingeras, STAR: ultrafast universal RNA-seq aligner. *Bioinformatics*. **29**, 15–21 (2013).

68. Y. Liao, G. K. Smyth, W. Shi, The R package Rsubread is easier, faster, cheaper and better for alignment and quantification of RNA sequencing reads. *Nucleic Acids Res.* **47**, e47–e47 (2019).

69. M. I. Love, W. Huber, S. Anders, Moderated estimation of fold change and dispersion for RNA-seq data with DESeq2. *Genome Biol.* **15**, 550 (2014).

70. A. Caballé-Mestres, A. Berenguer-Llergo, C. Stephan-Otto Attolini, Roastgsa: a comparison of rotation-based scores for gene set enrichment analysis. *BMC Bioinformatics*. **24**, 408 (2023).

Acknowledgments

We thank E. Bach, J. Castelli-Gair, N. Tapon, M. Suzanne, G. Juhasz, the Bloomington *Drosophila* Stock Center (USA), the Vienna *Drosophila* Resource Center (Austria), and the Developmental Studies Hybridoma Bank (USA) for flies and antibodies, and IRB Barcelona's Advanced Digital Microscopy, Functional Genomics, and Biostatistics and Bioinformatics Facilities for help. This work was funded by the *PID2019-110082GB-I00* and PID2022-137673NB-I00 grants from the Spanish Ministry of Science, Innovation and Universities (MICIU) and the ERDF "Una manera de hacer Europa", and the European Union's Horizon 2020 research and innovation programme under the Marie Skłodowska-Curie grant agreement number 945352. We gratefully acknowledge institutional funding from the MICIU through the Centres of Excellence Severo Ochoa Award, and from the CERCA Programme of the Catalan Government.

Author Contributions

All the authors conceived and designed the experiments and analysed the data. K.G. and A.K. performed the experiments, M.M. and K.G. prepared the final figures, and M. M. supervised the whole project and wrote the paper.

Declaration of interests

The authors declare no competing interests.

Figures

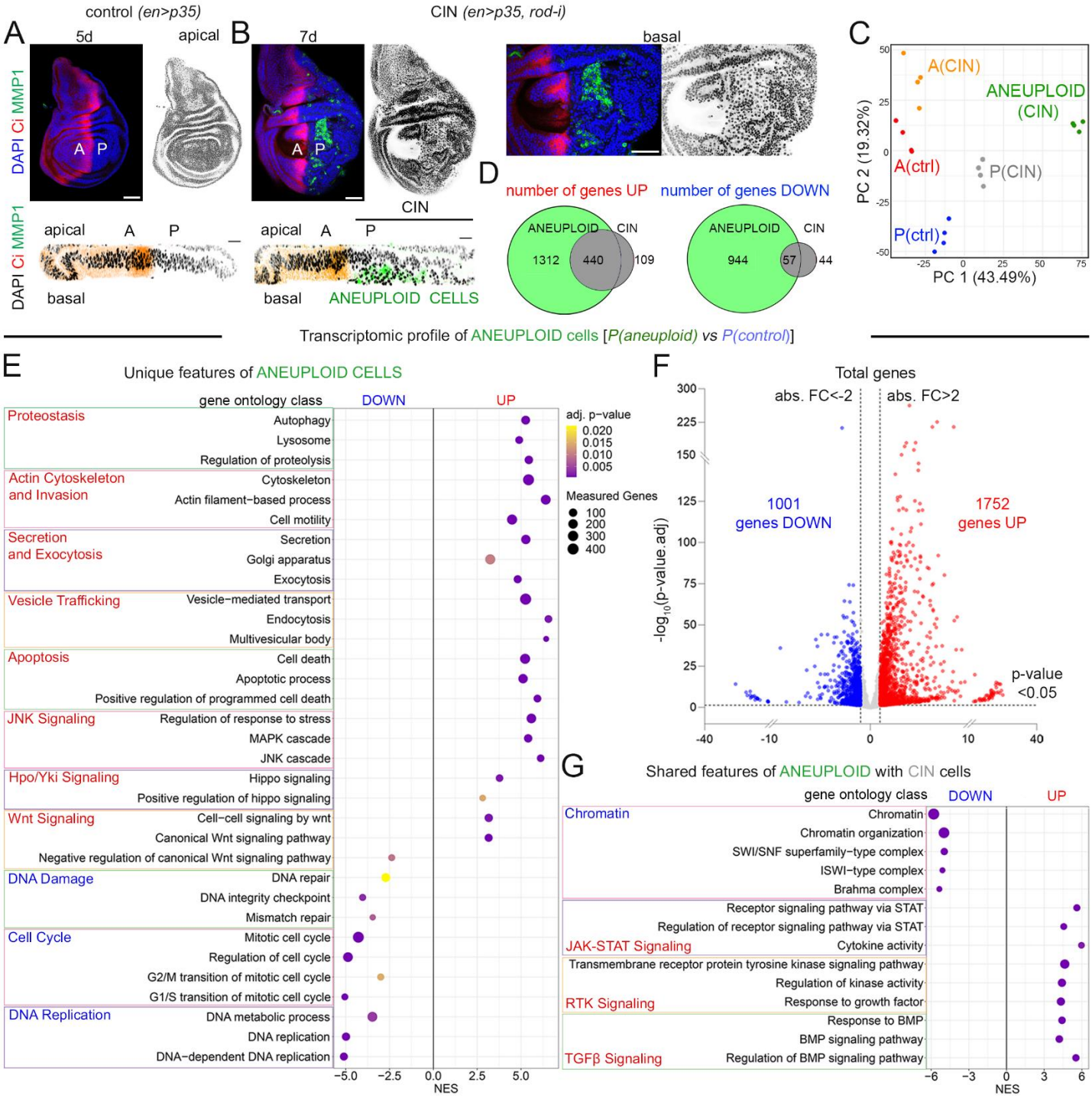

Figure 1. A distinct transcriptomic profile of aneuploidy-induced senescent cells

(A, B) Control wing discs (**A**) and wing discs subjected to CIN (**B**), stained for DAPI (blue or black), Ci (red, to label the A compartment), and MMP1 (green, to label the aneuploid cells) and expressing the indicated transgenes in the P compartment under the control of the *en-gal4* driver. Scale bars, 50 µm**.** Days of dissection after egg laying are as indicated. **(C)** Principal Component (PC) analysis showing the transcriptomic differences between the 5 different populations: A (Red) and P (Blue) cells of control wing discs, and aneuploid (green), A (orange) and P (gray) cells of wing discs subjected to CIN. **(D)** Venn diagram representing the number of genes up- or down-regulated uniquely in aneuploid cells (green), and proliferating cells subjected to CIN cells or in both types of cells (gray). **(E, G)** Bubble plots representing Gene Ontology (GO) enrichment analyses of aneuploid (**E**) and aneuploid and proliferating cells (**G**) when compared to P cells of control discs. Size of the bubble represents the number of measured genes, and the colour scale represents the associated p-value. **(F)** Volcano plot representing all the genes that are differentially up- (red dots, FC>2 and p-value<0.05) or down-regulated (blue dots FC<-2 and p-value<0.05), or not differentially expressed (gray dots, p-value>0.05 or 2>FC>-2) in aneuploid cells when compared to P cells of control discs. See also Figure S1, S2, and Table S1.

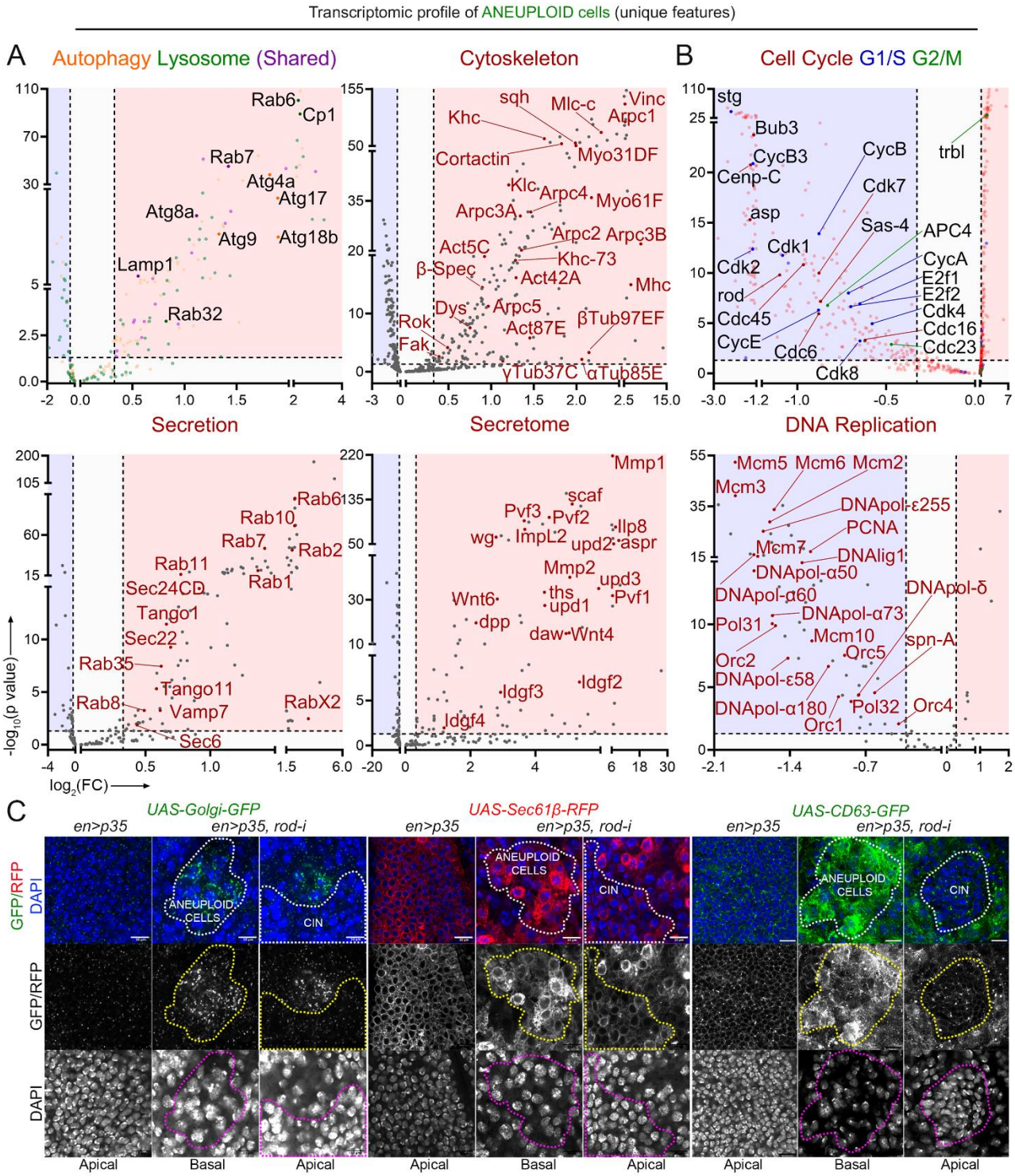

722 **Figure 2. The transcriptome of aneuploidy-induced senescent cells points to a heightened**

723 **secretory potential**

(A, B) Volcano plot representing GO class-specific genes that are differentially upregulated (red area, FC>2 and p-value<0.05), downregulated (blue area, FC<-2 and p-value<0.05), or not differentially expressed (white area, p-value>0.05 or 2>FC>-2) in aneuploid cells when compared to P cells of control discs. GO classes (A): Autophagy - GO0006914, Lysosome - GO0005764, Cytoskeleton - GO0005856, Secretion - GO0046903, Secretome - Custom Gene Set. GO classes (B): G1/S Transition - GO0000082, G2/M Transition - GO0000086, Regulation of cell cycle - GO0051726, and DNA Replication - GO0006260. Genes corresponding to each of the GO classes have a distinct colour code. **(C)** High magnification images of wing discs expressing the indicated transgenes under the control of the *en-gal4* driver and stained to visualize differential expression of fluorescent reporters (green, red, or white) and DAPI (blue and white). Apical and basal sections are shown. Aneuploid and CIN cells are marked by a dashed line. Scale bars, 10 µm**.** See also Tables S1 and S2.

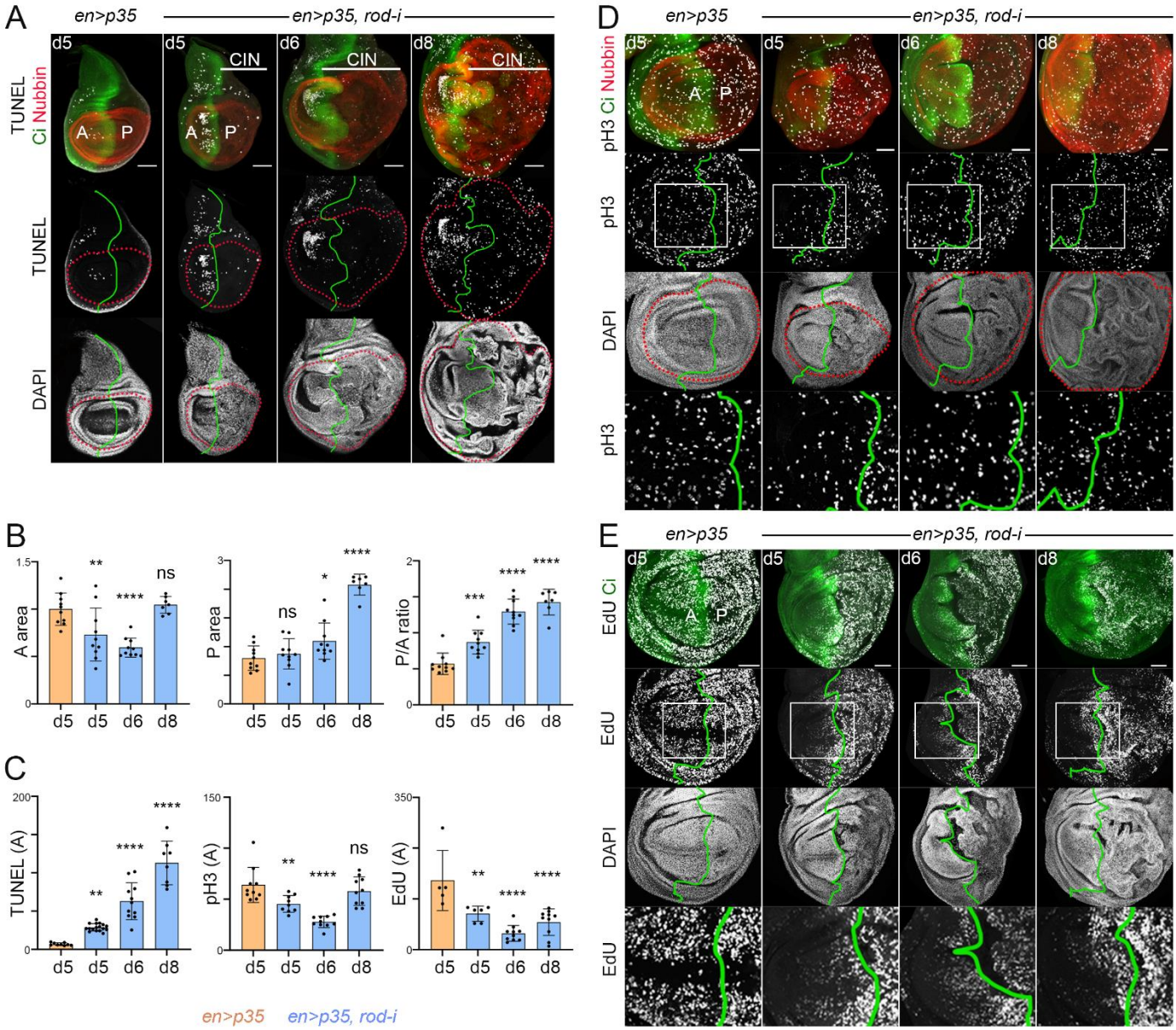

Figure 3. A non-autonomous effect of CIN tumours on the proliferation, growth, and survival of the neighbouring tissue

(**A**, **D**, **E**) Control wing discs (first column) and wing discs subjected to CIN (remaining columns), and expressing p35 in the P compartment under the control of the *en-gal4* driver, stained for Ci (green, to label the A compartment), DAPI (white), Nubbin (red, to label the wing pouch cells, **A**, **D**), TUNEL (white, **A**), pH3 (white, **D**), and EdU (white, **E**). Scale bars, 50 µm**.** Days of dissection after egg laying are as indicated. The boundary between A and P cells is labelled by a green line. The tissue subjected

to CIN is marked in **A**. High magnification of the squared regions is shown in the lower panels in **D**, **E**. Note the non-autonomous induction of cell death (**A**) and block of cell proliferation (**D**, **E**) in A cells. (**B**, **C**) Histograms plotting in **B** the normalized size of the wing pouch A and P compartments and the size ratio between these compartments, and in **C** the amount of TUNEL, pH3, and EdU incorporation in the A wing pouch compartment (normalized to the size of the corresponding compartment) of wing discs expressing the indicated transgenes in the P compartment under the control of the *en-gal4* driver. Ordinary one-way ANOVA was performed to analyse the data plotted in **B** and **C**. *$p<0.05$; **$p<0.01$; ***$p<0.001$; **** $p<0.0001$; ns, not significant. See also Figure S3 and Table S3.

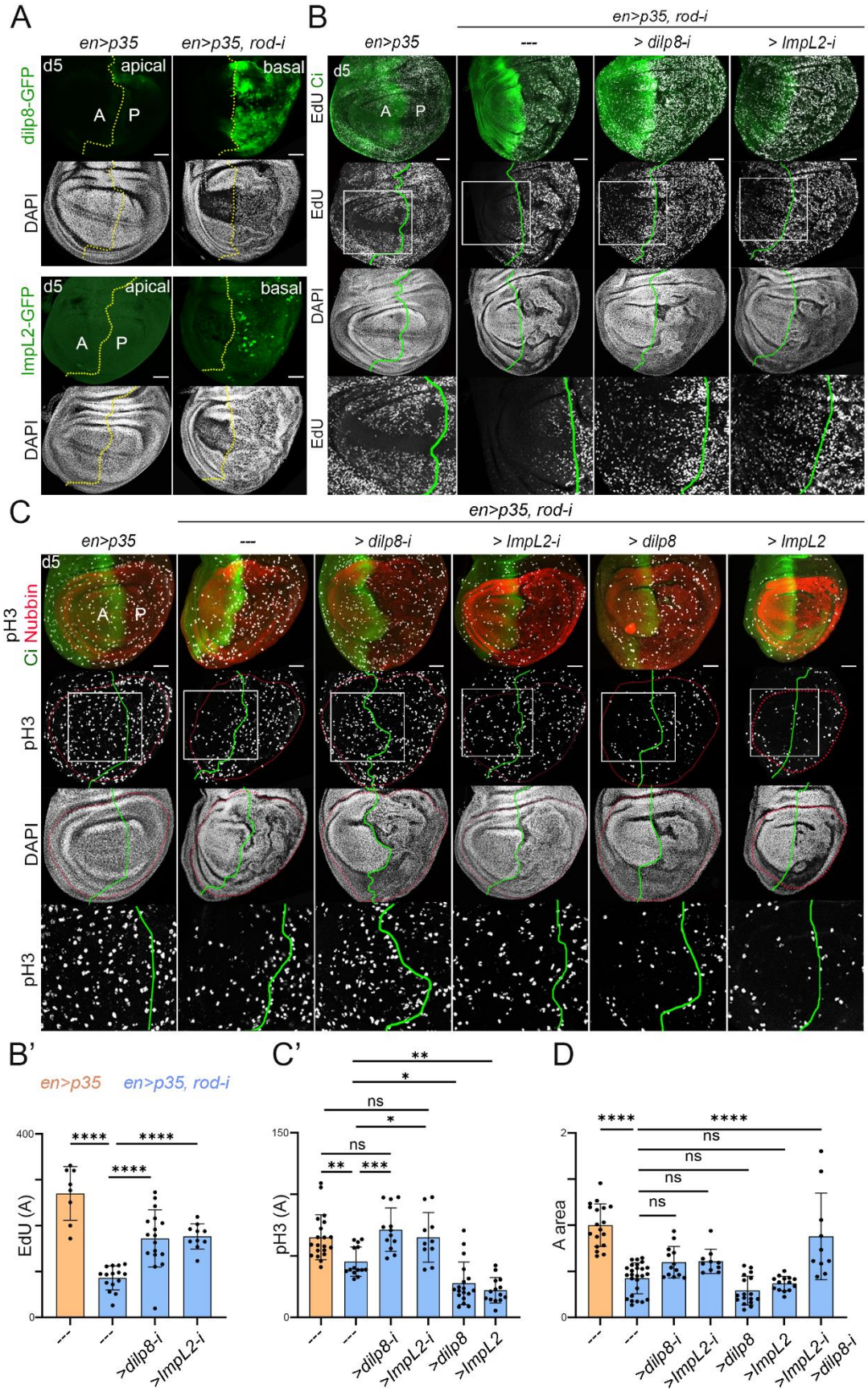
A
en>p35
en>p35, rod-i
d5
apical
basal
A
P
dilp8-GFP
DAPI
ImpL2-GFP
B
en>p35, rod-i
en>p35

> dilp8-i
> ImpL2-i
EdU Ci
EdU
C
en>p35, rod-i
> dilp8
> ImpL2
pH3
Ci Nubbin
B'
en>p35
en>p35, rod-i
EdU (A)
C'
pH3 (A)
D
A area
>dilp8-i
>ImpL2-i
>dilp8
>ImpL2
ns

752

Figure 4. Dilp8/Relaxin and ImpL2/IGFBP7 contribute to the non-autonomous effect of CIN tumours on the proliferation of the neighbouring tissue

(**A**-**C**) Control wing discs (first column) and wing discs subjected to CIN (remaining columns), stained to visualize Dilp8-GFP (green, **A**), ImpL2-GFP (green, **A**), EdU (white, **B**), pH3 (white, **C**), DAPI (white), Nubbin (red, to label the wing pouch cells, **C**), and Ci (green, to label the A compartment, **B**, **C**), and expressing the indicated transgenes in the P compartment under the control of the *en-gal4* driver. Scale bars, 50 µm**.** Discs were dissected 5 days after egg laying. The boundary between A and P cells is labelled by either a green line or a yellow dashed line. High magnifications of the squared regions are shown in the lower panels in **B**, **C**. Note the non-autonomous block of cell proliferation in A cells is partially restored upon *dilp8* or *ImpL2* depletion. (**B', C', and D**) Histograms plotting the amount of EdU incorporation and pH3 in the A wing pouch compartment (normalized to the size of the corresponding compartment, **B'**, **C'**), and the normalized size of the A wing pouch compartment (**D**) of wing discs expressing the indicated transgenes in the P compartment under the control of the *en-gal4* driver. Ordinary one-way ANOVA was performed to analyse the data plotted in **B', C' and D;** * $p<0.05$; ** $p<0.01$; *** $p<0.001$; **** $p<0.0001$; ns, not significant. See also Figure S4 and Table S3.

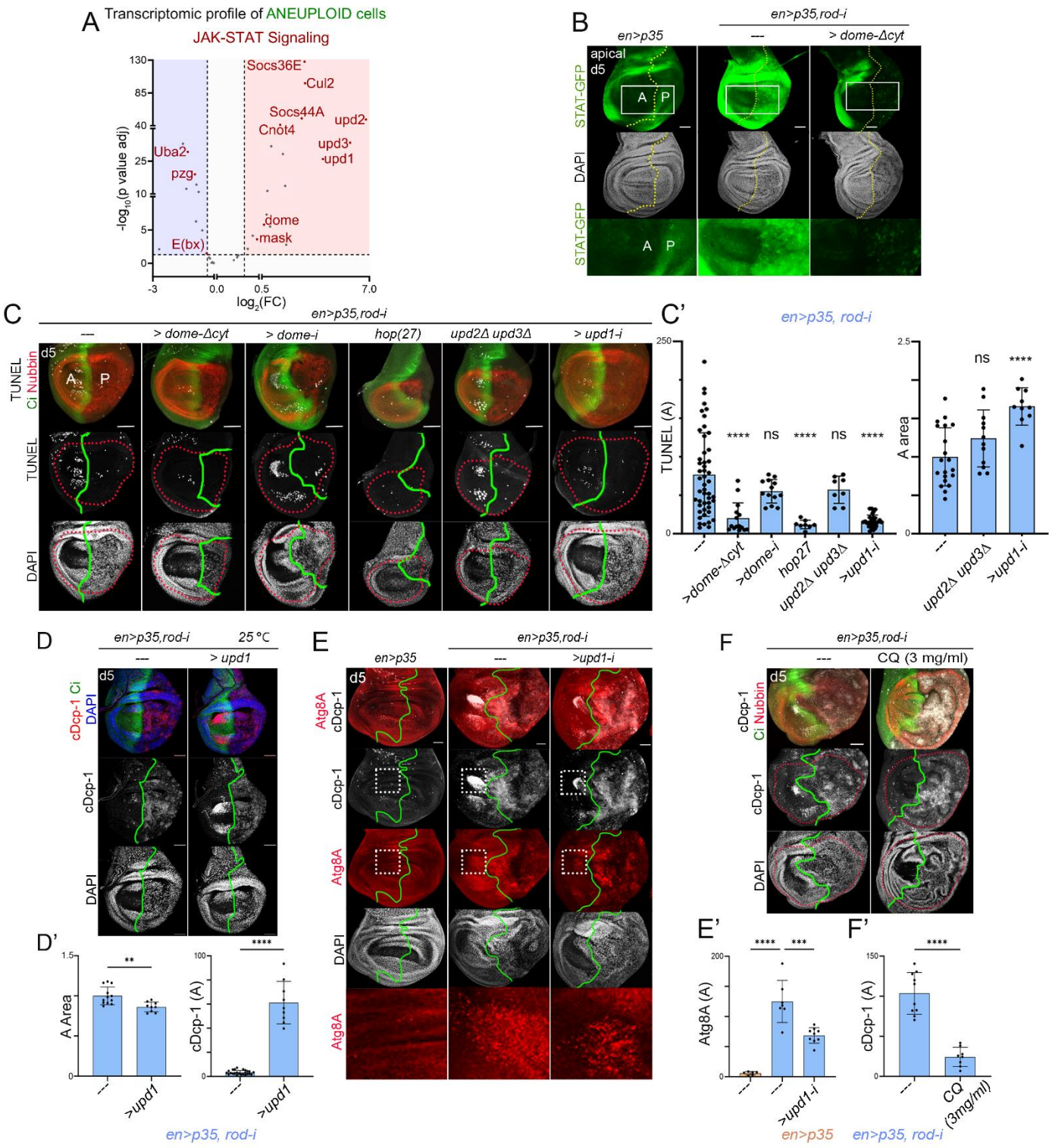

770 **Figure 5. Cytokine Upd1 contributes to the non-autonomous impact on cell death and growth**

(A) Volcano plot representing selected genes in JAK-STAT Signaling - GO0097696 class that are differentially upregulated (red area, FC>1.3 and p-value<0.05), downregulated (blue area, FC<-1.3 and p-value<0.05), or not differentially expressed (white area, p-value>0.05 or 1.3>FC>-1.3) in aneuploid cells when compared to P cells of control discs. (**B, C, D, E, F**) Control wing discs (first column in **B**, **E**) and wing discs subjected to CIN (remaining columns in **B, C, D, E, F**) stained to visualize STAT-GFP (green, **B**), TUNEL (white, **C**), cDcp-1 (red and white, **D**; white, **E**, **F**), mCherry-Atg8 (red, **E**), DAPI (white or blue, **D**), Nubbin (red, to label the wing pouch cells, **C**, **G**), and Ci (green, to label the A compartment, **C, D and F**), and expressing the indicated transgenes in the P compartment under the control of the *en-gal4* driver. Larvae in **F** were subjected to chloroquine (CQ) feeding for 72 h. Scale bars, 50 µm**.** Discs were dissected 5 days AEL. The boundary between A and P cells is labelled by a green or a yellow dashed line. High magnification of the squared regions are shown in the lower panels in **B** and **E**. (**C', D', E', and F'**) Histograms plotting the amount of TUNEL (**C'**), cDcp-1 (**D'**, **F'**), or mCherry-Atg8 signal (**E'**) in the A wing pouch compartment (normalized to the size of the corresponding compartment), and the normalized size of the A wing pouch compartments (**C'**) or entire A compartments (**D'**) of wing discs expressing the indicated transgenes in the P compartment under the control of the *en-gal4* driver. Ordinary one-way ANOVA was performed to analyse the data plotted in **C', E'**. Unpaired t-test was performed to analyse the data plotted in **D', F'**. *p<0.05, **p<0.01, ***p<0.001, **** p<0.0001, ns, not significant. See also Figure S5 and Tables S1 and S3.

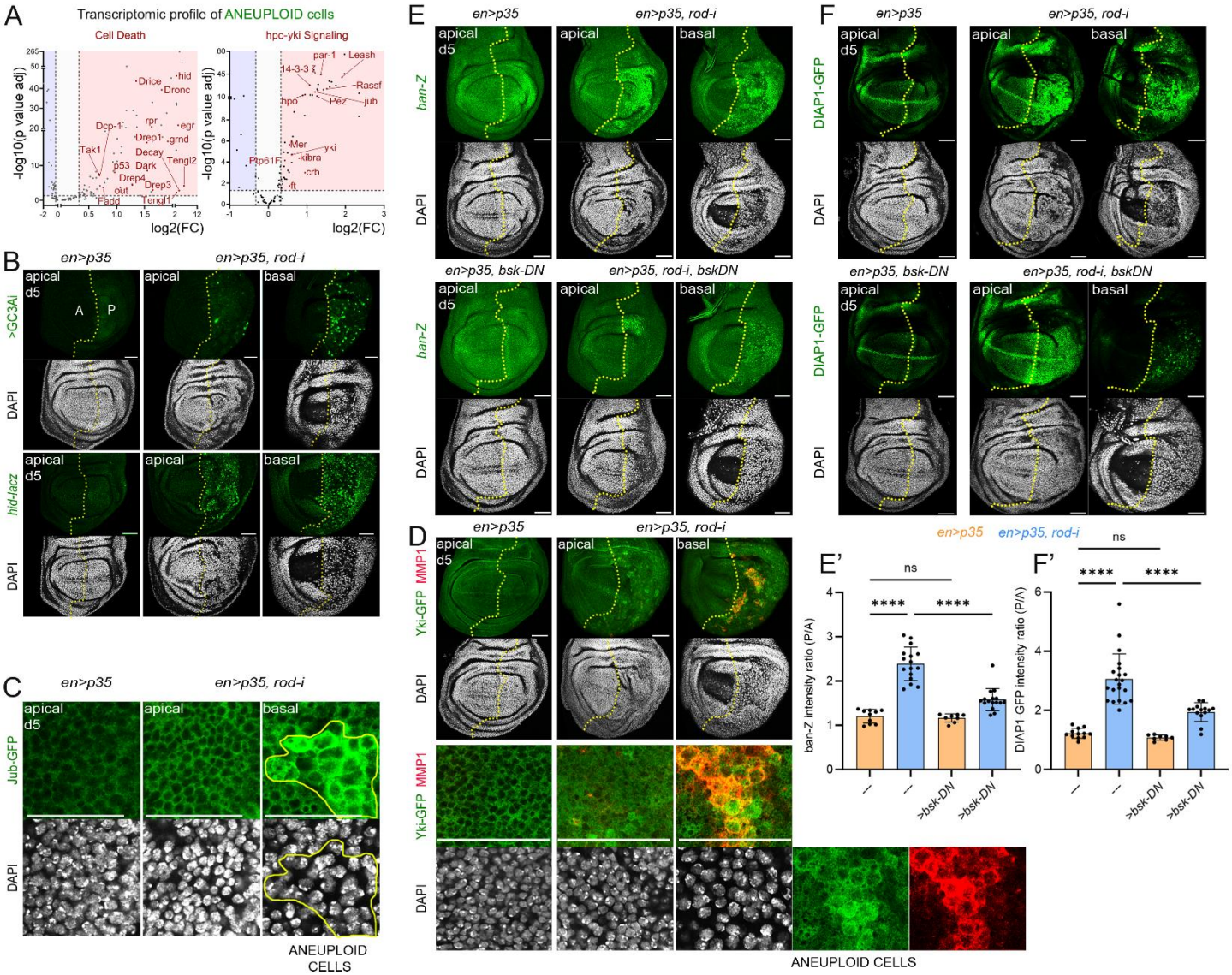

Figure 6. The transcriptome of aneuploidy-induced senescent cells points to activation of the apoptotic and Yorkie pathways

(A) Volcano plot representing selected genes in 'Cell death - GO0008219' (left), and 'hpo-yki signaling - GO0035329' (right) classes that are differentially upregulated (red area, FC>1.3 and p-value<0.05), downregulated (blue area, FC<-1.3 and p-value<0.05), or not differentially expressed (white area, p-value>0.05 or 1.3>FC>-1.3) in aneuploid cells when compared to P cells of control discs. (**B**-**F**) Control wing discs (first column) and wing discs subjected to CIN (remaining columns), stained to visualize GC3Ai or *hid-lacZ* (green, **B**), Jub-GFP (green, **C**), Yorkie-GFP (green, **D**), *bantam-lacZ*

(green, **E**), DIAP1-GFP (green, **F**), DAPI (white, **B**-**F**), MMP1 (red, **D**), and expressing the indicated transgenes in the P compartment under the control of the *en-gal4* driver. In **C**, aneuploidy-induced senescent cells are marked by a yellow line. Scale bars, 50 µm**.** Discs were dissected 5 days AEL. The boundary between A and P cells is labelled by a yellow line. Note in **E** and **F,** a reduction in the expression levels of *bantam-lacZ* and *DIAP1-GFP* upon expression of a dominant negative form of JNK (Bsk-DN). (**E'**, **F'**) Histograms plotting the P/A signal intensity ratio of *bantam-lacZ* (**E'**) and *DIAP1-GFP* (**F'**) of wing discs expressing the indicated transgenes in the P compartment under the control of the *en-gal4* driver. Ordinary one-way ANOVA was performed to analyse the data. *$p<0.05$, **$p<0.01$, ***$p<0.001$, **** $p<0.0001$, ns, not significant. See also Table S3. See also Figure S6 and Tables S1 and S3.

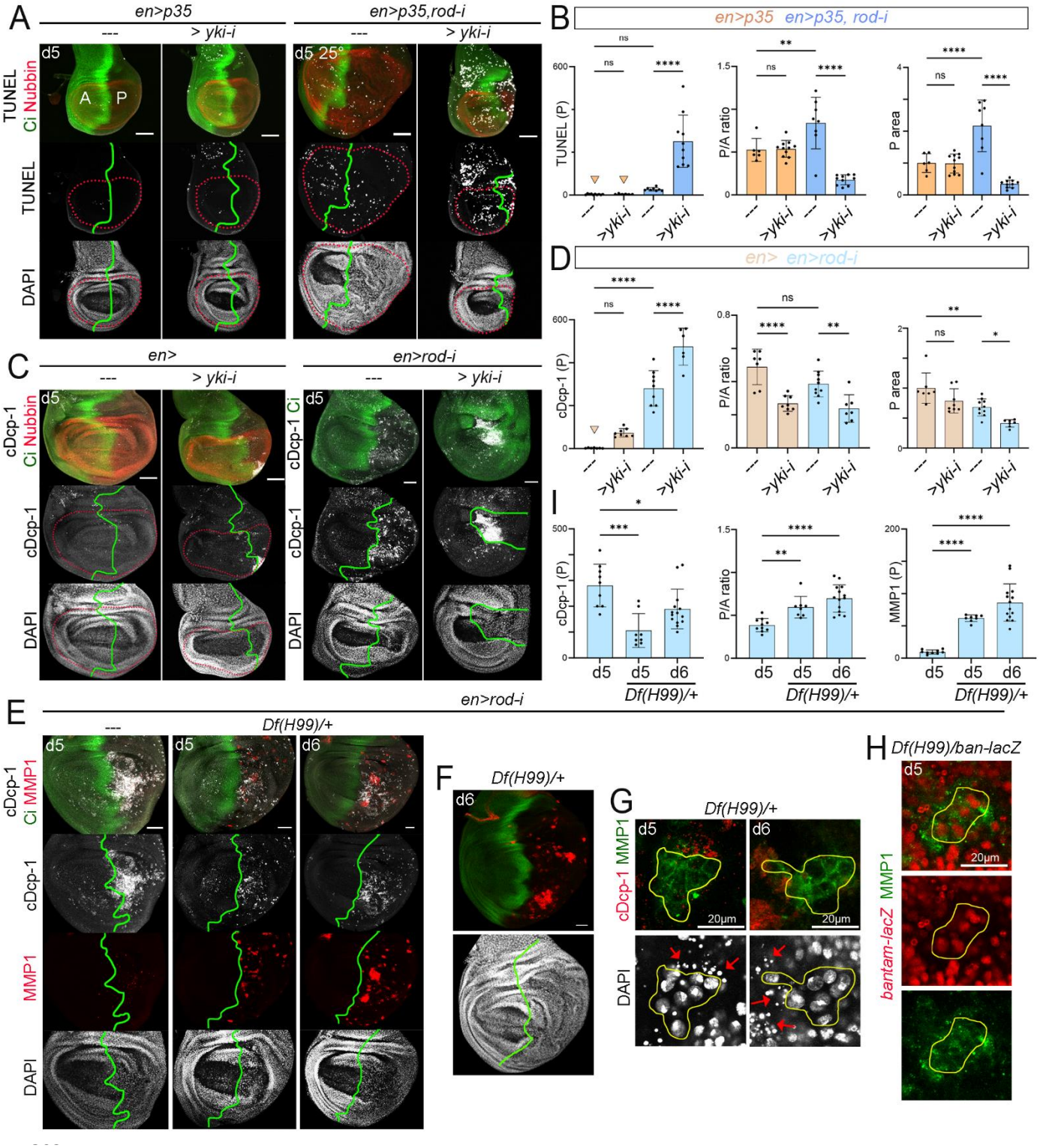

Figure 7. Yorkie plays a pro-survival role in CIN tissues

(**A, C, E, F, G, H**) Control wing discs (first columns in **A**, **C**) and wing discs subjected to CIN (remaining columns), stained to visualize TUNEL (**A**, white), cDcp-1 (**C**, **E**, white, **G**, red), *bantam-lacZ* (red, **H**), Ci (green, **A**, **C**, **E, F**), Nubbin (red, **A**, **C**), MMP1 (red, **E**, green, **G**, **H**), and DAPI (white, **A, C, E, F, G**) expressing the indicated transgenes in the P compartment under the control of the *en-gal4* driver. Scale bars, 50 µm, unless indicated otherwise**.** Discs were dissected at the indicated days of development. The boundary between A and P cells is labelled by a green line, and the wing pouch by a red dotted line. In **G**, **H**, high magnification images of the basal sections of CIN tissues, where aneuploidy-induced senescent cells are found and marked by a yellow line. (**B**, **D**, **I**) Histograms plotting the amount of TUNEL (**B**, left), MMP1 (**I,** right) and cDcp-1 signal (**D, and I,** left) in the P wing pouch compartment (normalized to the size of the corresponding compartment), the normalized size of the P wing pouch compartment (**B**, **D**, right), and size ratio between the P and A wing pouch compartments (**B, D and I,** centre) of wing discs expressing the indicated transgenes in the P compartment under the control of the *en-gal4* driver. Ordinary one-way ANOVA was performed to analyse the data plotted in **B, D, I;** * $p<0.05$, ** $p<0.01$, *** $p<0.001$, **** $p<0.0001$, ns, not significant. See also Figure S7 and Table S3.

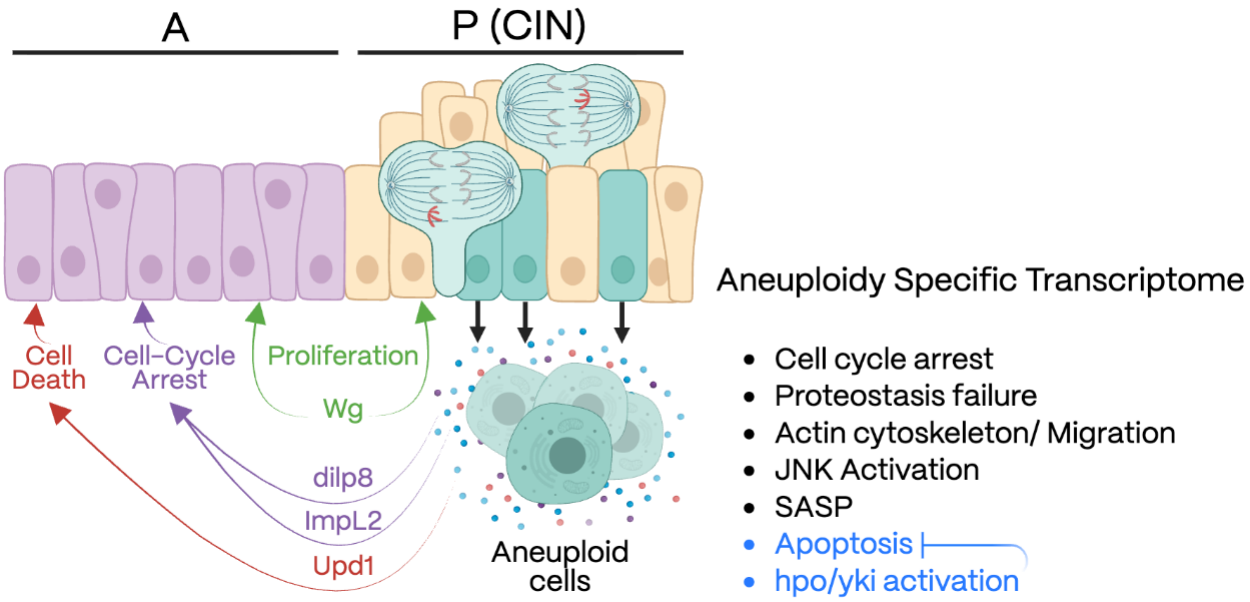

Figure 8. Aneuploidy-specific transcriptome, interactions with the TME through the SASP and a pro-survival role of Yorkie

In epithelial tissues subjected to restricted induction of CIN in the P cell population (yellow), aneuploid cells (green) delaminate basally and enter a senescent state. The cellular responses to aneuploidy-induced senescence are reflected at the transcriptional level, including cell cycle arrest, proteostasis failure, a highly migratory phenotype, JNK activation and a SASP consisting of more than 40 secreted proteins. Members of the SASP, including Wg, Dilp8/Relaxin, ImpL2/IGFBP-7 and Upd1, impact on the neighbouring TME (the A cell population depicted in pink) to induce cell death and regulate cell proliferation and growth. Hippo/Yorkie signalling is induced in aneuploidy-induced senescent cells to block apoptosis. Cartoon was generated with Biorender.com.

838 **Tables**

#	Symbol	Gene name	Vertebrate homolog	Significance (p. value)	Fold Change
1	*RYa*	*Ryamide*	*NPY family*	3.13E-08	3.01E+07
2	*Diedel3*	*Diedel 3*	*LGALS3BP*	4.96E-06	4.99E+05
3	*CG11211*	Unannotated		2.08E-06	4.80E+05
4	*nec*	*necrotic*	*SERPIN*	1.04E-51	30.33
5	*NLaz*	*Neural Lazarillo*	*ApoD and RBP4*	6.83E-13	22.47
6	*PGRP-SA*	*Peptidoglycan recognition protein SA*	*PGLYRP3*	1.23E-30	20.32
7	*sona*	*sol narae*	*ADAMTS*	4.04E-70	16.55
8	*aspr*	*asperous*	*DNER and EDIL3*	4.95E-15	16.16
9	*CG30280*	Unannotated	*MFAP4*	1.84E-04	15.84
10	*Pvf1*	*PDGF- and VEGF-related factor 1*	*PDGF and VEGF*	1.22E-13	14.07
11	*Mmp1*	*Matrix metalloproteinase 1*	*MMP*	6.01E-71	12.36
12	*scaf*	*scarface*	*Serine Protease*	7.64E-63	12.08
13	*Wnt4*	*Wnt oncogene analog 4*	*WNT*	1.21E-09	12.06
14	***Ilp8***	***Insulin-like peptide 8***	***Relaxin***	**7.09E-20**	**11.88**
15	*Mmp2*	*Matrix metalloproteinase 2*	*MMP*	3.39E-20	10.93
16	*Tig*	*Tiggrin*	*RGD-containing integrin ligand*	3.19E-09	9.74
17	*upd3*	*unpaired 3*	*Il-6*	1.35E-10	7.89
18	*upd2*	*unpaired 2*	*Leptin*	1.09E-10	7.37
19	***upd1***	***unpaired 1***	***Il-6***	**1.24E-13**	**7.32**
20	*CG31869*	Unannotated		2.04E-40	7.15
21	*Idgf2*	*Imaginal disc growth factor 2*	*CHI3L1, CHI3L2, and OVGP1*	2.98E-04	6.51
22	*CG9095*	Unannotated		3.28E-12	6.35
23	*ths*	*thisbe*	*FGF8*	1.89E-13	5.80
24	*Spn47C*	*Serpin 47C*	*SERPIN*	3.08E-23	5.68
25	*CG1136*	Unannotated		5.74E-05	5.68
26	*Fs*	*Follistatin*	*FSTL*	3.54E-17	5.53
27	*mtg*	*mind the gap*	*Lectin*	2.90E-39	5.50
28	*Spn55B*	*Serpin 55B*	*SERPIN*	9.41E-46	5.49
29	*Sp7*	*Serine protease 7*	*Serine Proteases*	7.98E-17	5.48
30	*spz5*	*spatzle 5*	*Neurotrophin*	1.98E-03	5.47
31	***wg***	***wingless***	***WNT***	3.13E-47	5.33
32	*tnc*	*tenectin*	*Mucin-type protein with RGD motif*	2.25E-05	5.29
33	*CG13618*	Unannotated		2.80E-10	5.11

34	*fon*	*fondue*	*NCOA5 and NUP98*	2.13E-05	5.06
35	*Wnt6*	*Wnt oncogene analog 6*	*WNT*	5.94E-21	4.97
36	*Pvf2*	*PDGF- and VEGF-related factor 2*	*PDGF and VEGF*	2.27E-26	4.60
37	*frm*	*farmer*	*FLG*	4.79E-29	4.48
38	*eys*	*eyes shut*	*EYS*	3.81E-05	4.45
39	*CG14301*	Unannotated		3.54E-16	4.28
40	*CG10031*	Unannotated		2.91E-03	4.26
41	*CG3604*	Unannotated		4.92E-04	4.25
42	*orion*	*orion*	Chemokine-like	2.97E-25	4.18

Table 1. The secretome of the aneuploidy-induced senescent cells.

Table representing 42 out of the 250 most differentially upregulated genes (comparing the transcriptome of the aneuploidy-induced senescent cells with those of the P(CIN) cells) which are annotated as genes encoding for secreted proteins, along with their vertebrate homolog, adjusted p. values and shrunken fold-changes. The genes labelled in red are those which have been mentioned in the current work. A manually curated custom gene set, consisting of 261 known or predicted secreted proteins as inferred from FlyBase is provided in Table S2. The transcriptome of the aneuploidy-induced senescent cells was compared to the P(CIN) cells in order to identify those secreted proteins which are specific to aneuploidy-induced senescent cells and not expressed as a general consequence of tumour induction